# Unknown input uncertainty calculation using virtual input shaping and interval analysis.

Sylvain Hernandez[a,•,1], Emmanuel Piat[a], Joël Abadie[a], Eric Lesniewska[b]

[a] : Department of Automatic Control and Micro-Mechatronic Systems, FEMTO-ST Institute, CNRS UMR 6174, University Bourgogne Franche-Comté, 24 rue Alain Savary, 25000 Besançon, France.
[b] : Department of Nanosciences, ICB, CNRS UMR 6303, University Bourgogne Franche Comté, 9 Avenue Alain Savary, 21078 Dijon, France.

*Email addresses :*

- sylvain.hernandez2@femto-st.fr (Sylvain Hernandez)

- emmanuel.piat@ens2m.fr (Emmanuel Piat)

- joel.abadie@femto-st.fr (Joël Abadie)

- eric.lesniewska@u-bourgogne.fr (Eric Lesniewska)

• : Corresponding author.

1 : Permanent address : sylvain.hernandezsabio@gmail.com

## Highlights

- Equivalent representation of a nonlinear system by a linear model with a virtual input;

- Virtual input shaping to distinguish quantities of interest from measurement biases;

- Uncertainty propagation by solving inverse problem using interval analysis;

- Simulation of a passive triaxial pendulum accelerometer in different scenarios.

## Keywords

- Nonlinear system representation;

- Unknown input estimation;

- Dynamic measurement uncertainty;

- Virtual input shaping;

- Interval Analysis;

- SIVIAP algorithm.

### Abstract

A triaxial accelerometer has been developed to measure and determine the uncertainty associated with unknown vibrations disturbing a small force metrology experiment. However, methodological shortcomings remain regarding the calculation of uncertainty for dynamic measurements. Therefore, this paper proposes an alternative framework to estimate the uncertainty of specific dynamic quantities of interest with a nonlinear and uncertain measuring system. The novelty of the proposed methodology lies in the use of an accurate and equivalent representation of the physical system based on a linear model, combined with an additive virtual input describing all the unknown unmodeled dynamics. Measurement models are defined considering measurement biases, and uncertainty is calculated using interval analysis tools. Such tools allow determining the feasible values of the quantities of interest to be estimated. The innovative aspects of the proposed approach are fully illustrated in simulation on the triaxial accelerometer, comparing linear and nonlinear measurement models in passive mode.

# 1 Introduction

Nowadays, measurement of small forces is encountered in a large panel of scientific applications, such as the design of micro-thruster for miniaturized spacecraft [1], the characterization of the mechanical properties of micro-electromechanical systems (MEMS) by nanoindentation [2] or the study with atomic force microscopes (AFMs) of biological material like DNA [3]. The range of forces involved in these fields extends from approximately one newton (N) to a few piconewton (pN). However, the measuring instruments used do not benefit from an appropriate calibration procedure, as there are no small force standards at these scales. Indeed, National Metrology Institutes (NMIs) are not able to officially guarantee the traceability of measurements below 0.1 N at the international level[1], according to the database (KCDB) of their mutual recognition agreement. Therefore, NMIs and research laboratories put a lot of efforts in the development of reference standards [4, 5, 6], such as electrostatic force balances [7, 8], and transfer artifacts [9, 10, 11] to tackle this issue and to give credibility to the scientific activities concerned.

In this context, an electromagnetic microforce balance traceable to the International System of Units (SI) is being developed based on an existing force generator [12], for potential use as a force reference standard. This device operates inside a vacuum chamber placed on a table equipped with a vibration isolation system. Nevertheless, seismic activity is not fully filtered resulting in unknown inertial forces that disturb the dynamics of the microforce balance, which has a bandwidth of a few hertz. Instead of considering them as an unknown random noise, this residual low-frequency signal needs to be measured. Indeed, the magnitude of these inertial forces is significant at this scale and can no longer be neglected when studying the dynamics of the small force balance. On top of that, this vibratory regime is not necessarily steady, and might present significant transients in practice if experimental conditions are poorly controlled. A highly sensitive reference system is therefore required alongside the force balance to provide an accurate estimate of the disturbing inertial forces [13, 14], and measurement uncertainty. The internal mechanisms - such as mechanical structure, signal conditioning, systematic and random error compensation - of an accelerometer purchased directly on the market would not necessarily be known. A laboratory trixial accelerometer, simple at first sight, has therefore been expressly designed to meet the specifications imposed by the force balance. This development motivated in-depth research into how the uncertainty of inertial force measurements can be efficiently estimated with this device.

As regards uncertainty calculation, scientists generally refer to the official guidelines written in the Guide to the expression of Uncertainty in Measurement (GUM) [15] and its supplements [16, 17, 18]. However, inconsistencies have been highlighted by the scientific community. The committee in charge of this guide has recognized that the Bayesian approach introduced in the supplements is more appropriate to cal-

---

[1]Taken from the official BIPM website : `https://www.bipm.org/kcdb`

culate uncertainty than the frequentist approach initially used in the GUM. Therefore, a complete revision is considered based on the Bayesian inference [19]. The GUM also presents methodological shortcomings as regards uncertainty calculation for time-dependent quantities measured with dynamical systems. Guidelines for such dynamic measurements have been introduced in the latest supplement, but only linear and time-invariant (LTI) measuring systems are considered. In this case, the response of the system should be modeled in order to determine its input quantities based on its transfer function in the frequency domain, or using a digital deconvolution filter in the time domain. Uncertainty is then calculated using the Law of Propagation of Uncertainty (LPU) or Monte Carlo methods. However, the generalization of this procedure to a large number of systems faces challenges that still need to be resolved to further improve the metrology related to dynamic measurements [20]. A closer look at different disciplines, where the case of dynamical systems is more common, such as signal processing and automation, is suggested [21]. In Automation, state-space representations are often used to describe dynamical systems as a function of state variables. These variables correspond to specific quantities used to model the system behavior in response to given inputs. Usually, observers are implemented to estimate in real-time their evolution, based on the input-output signals of the system and a model of it. Since the first linear observers designed by Kalman for stochastic systems [22] and by Luenberger for deterministic systems [23], many developments have been made to handle several classes of nonlinear dynamical systems [24, 25, 26, 27, 28]. Initially intended for robust control purposes, observer structures of interest for uncertain systems have also emerged for estimating unmodeled dynamics and external disturbances, which more generally refer to unknown inputs [29, 30, 31]. The cited articles are not exhaustive and represent only a small part of the huge amount of work carried out in this field.

The above-mentioned accelerometer consists of three separate single-axis accelerometers oriented orthogonally in space. Each accelerometer corresponds actually to a dynamical single-input single-output (SISO) system exposed to external disturbances, including the unknown residual vibrations. Recently, an exact manner of representing the true behavior of a specific class of dynamical SISO systems despite the presence of multiple unknown inputs, has been developed [32]. All the unknown inputs are lumped together on the control input channel of the system, in a quantity called virtual input which is estimated by an Extended State Observer (ESO) [33]. This concept of equivalent modeling is in line with existing approaches [34, 35] that seek robust control laws for disturbed dynamical systems based on their input and output signals, rather than on mathematical models. This paradigm provides an interesting basis for estimating the unknown vibrations with the triaxial accelerometer. Indeed, the exact behavior of the system would be accurately reproduced, and all unmodeled dynamics and external disturbances, such as residual vibrations to be estimated, would be included in the virtual input. However, there is no connection between the approach described in [32] and uncertainty calculation, which makes it of little interest for metrological applications. This paper is therefore a proposal aimed at filling this gap, and extending the scope of the equivalent representation concept to

4

the metrology of nonlinear dynamical systems.

The article is structured as follows. Section 2 is devoted to presenting the theoretical framework of the proposed approach. Section 2.1 presents the theorem of equivalent representation based on the notion of virtual input. On this basis, Section 2.2 develops the problem of virtual input shaping. The observation of the virtual input and the determination of its proper uncertainty are developed in Section 2.3. Section 2.4 introduces the calculation of uncertainty intervals associated to the quantities of interest using interval analysis. These four steps are illustrated by simulations on the triaxial accelerometer in Section 3. The complete system is simulated in passive mode with parametric uncertainties, in response to different excitation signals to compare linear and nonlinear measurement models. The limitations and outlooks of this work are presented in Section 4.

# 2    Presentation of the methodology

The methodology developed in this part is schematized in Fig. 1 and is summarized to give an overview. The quantities of interest to be estimated are denoted by $Q$ on the left side of the figure. They are part of the external disturbances $d$ that affect the behavior of the nonlinear system $(\mathcal{S})$ located in the red overlay. These quantities of interest cannot be measured directly and must therefore be deduced from knowledge of $(\mathcal{S})$ using a linear model $(\mathcal{M})$, but also from the remaining disturbances in $d$. The effective input-output signals $u$ and $y$ of $(\mathcal{S})$ may differ respectively from the numerical values $\mathrm{u}^c$ and $\mathrm{y}^m$ due to potential imperfections in the actuation and measurement chains, such as electronic noise or conversion error. The uncertainty associated is therefore taken into account in the calculation by considering intervals $[\mathrm{u}^c]$ and $[\mathrm{y}^m]$. Similarly, uncertainty intervals can be introduced for uncertain parameters involved in the modeling of system $(\mathcal{S})$. The disturbances remaining in $d$ that can be measured are called measurement biases, to be consistent with the vocabulary of metrology, and are denoted by $D$. The interval $[\mathrm{D}^m]$ corresponds to measurements with a given uncertainty of these experimental biases. Therefore, the model $(\mathcal{M})$, the quantities $[\mathrm{u}^c]$, $[\mathrm{y}^m]$, $[\mathrm{D}^m]$ and the uncertain parameters constitute the inputs for the computation stages of the process in the green and yellow overlays. The following sections describe each stage of this methodology in detail.

## 2.1    Step one: Equivalent representation of uncertain systems

The specific class of systems considered in [32] to introduce the equivalent state-space representation is composed of time-varying nonlinear SISO systems, whose input-output dynamics is described by Ordinary Differential Equations (ODEs) of order $n > 0$, involving the $n - 1$ successive derivatives of the output $y$. However, this kind of external representation does not take into account potential internal variables. This is why the aforementioned approach is here extended to a more generic state-space framework to deal with internal representation. Consider $(\mathcal{S})$, a disturbed and
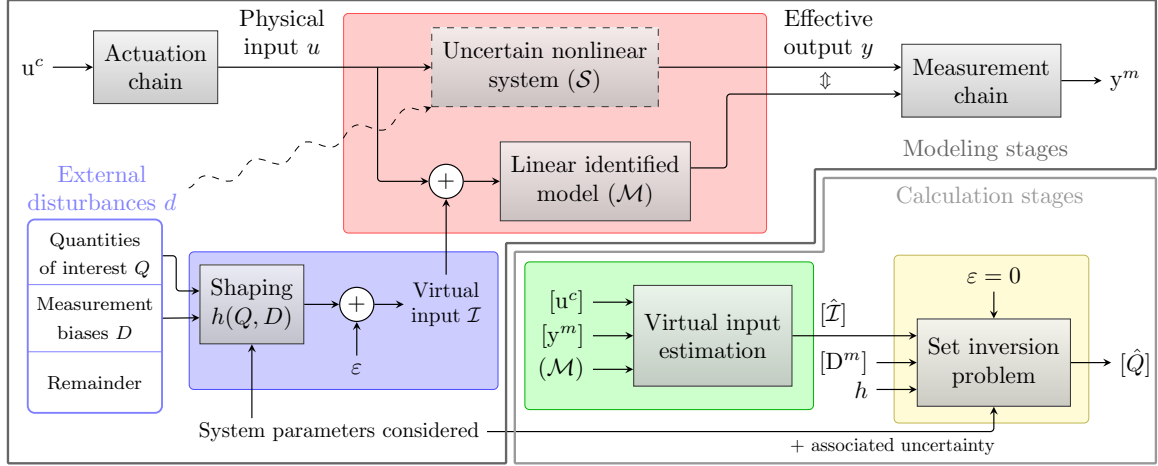
Figure 1: Schematic illustration of the proposed methodology.

possibly time-varying nonlinear SISO system whose dynamics is fully described by the following $n$-order state-space representation:

$$(\mathcal{S}) : \begin{cases} \dot{\mathcal{X}} = f(\mathcal{X}, u, d, t), \\ y = g(\mathcal{X}, u, d, t) \end{cases} \tag{1}$$

with

- $\mathcal{X} \in \mathbb{R}^n$ the system state vector;

- $u \in \mathbb{R}$ the controlled input of the system that is provided by the controller;

- $d \in \mathbb{R}^\delta$ the multidimensional continuous disturbance inputs that affect the system in any way;

- $f$ and $g$ the time-varying state evolution and output observation functions;

- $y \in \mathbb{R}$ the output of the system.

The existence of $f$, $g$, $\mathcal{X}$, $u$, $d$, $y$, $\delta$ and $n$ is assumed for the remainder of this study. In this article, the true dynamics of $(\mathcal{S})$ is therefore supposed to be accurately represented by the state-space representation (1).

Let $(\mathcal{M})$ be an approximate model of $(\mathcal{S})$ defined by the following linear state-space representation:

$$(\mathcal{M}) : \begin{cases} \dot{X}_m = AX_m + Bu, \\ y_m = CX_m \end{cases} \tag{2}$$

in which

6

- $X_m \in \mathbb{R}^p$ is a state vector of order $p > 0$, with no constraint on the value of $p$, made of fixed state components that are the modeled output $y_m$ and its $p - 1$ successive derivatives:

$$X_m = \begin{bmatrix} y_m & \dot{y}_m & \dots & y_m^{(p-1)} \end{bmatrix}^T \in \mathbb{R}^p; \tag{3}$$

  The subscripts $m$ indicate that these time-varying quantities are modeled quantities.

- $A$, $B$, $C$ are respectively the state, input and output companion matrices of $(\mathcal{M})$ defined by $p$ coefficients $a_i$ arbitrarily chosen, and a coefficient $b \neq 0$ such as:

$$A = \begin{bmatrix} 0 & 1 & 0 & 0 & \dots & 0 \\ 0 & 0 & 1 & 0 & \dots & 0 \\ & & & \ddots & & \\ 0 & 0 & 0 & \dots & 0 & 1 \\ -a_0 & & \dots & & -a_{p-1} \end{bmatrix}, \; B = \begin{bmatrix} 0 \\ 0 \\ \vdots \\ 0 \\ b \end{bmatrix}, \tag{4}$$

$$C = \begin{bmatrix} 1 & 0 & \dots & 0 \end{bmatrix}.$$

  The pair $(A, C)$ is observable.

On this basis, an equivalent representation of the input-output dynamic of $(\mathcal{S})$ can be obtained thanks to the following theorem.

**Theorem 1 (Equivalent representation)** *For any given nonlinear system $(\mathcal{S})$ defined by Equation (1) with $y(0), \dots, y^{(p-1)}(0)$ as initial conditions on its output, and for any given linear model $(\mathcal{M})$ defined by (2) with $X_m(0) = \begin{bmatrix} y(0) & \dots & y^{(p-1)}(0) \end{bmatrix}^T$, it exists a virtual input $\mathcal{I}(t)$ such that the nonlinear input-output dynamics of the couple $(u(t), y(t))$ can be equivalently represented by the following linear state-space equations:*

$$(\mathcal{S}) \Leftrightarrow \begin{cases} \dot{X} = AX + B(u + \mathcal{I}), \\ y = CX \end{cases} \tag{5}$$

*with $A$, $B$, $C$ the state, input and output matrices of $(\mathcal{M})$, and $X \in \mathbb{R}^p$ a state vector having the following components:*

$$X = \begin{bmatrix} y & \dot{y} & \dots & y^{(p-1)} \end{bmatrix}^T \in \mathbb{R}^p. \tag{6}$$

This theorem is proved in A, which expresses how $\mathcal{I}$ is causally defined. This additive input term is a mathematical construction that is homogeneous to the input control $u$ of the system $(\mathcal{S})$ and induces the dynamic of its output $y$ based on the structure of $(\mathcal{M})$. If the model $(\mathcal{M})$ is perfectly accurate, the virtual input $\mathcal{I}$ will be null. Otherwise, its absolute value will be modified so that $(\mathcal{M})$ corresponds exactly to the real output of $(\mathcal{S})$, taking into account the effects of modeling errors and external disturbances. Therefore, the virtual input $\mathcal{I}$ associated to $(\mathcal{M})$ is a time-valued

function which represents the discrepancy between the dynamics of the model $(\mathcal{M})$ and the system $(\mathcal{S})$. This first modeling stage corresponds to the red overlay in Fig. 1.

To illustrate this, let $\mathcal{X} = \begin{bmatrix} x_1 & x_2 & x_3 \end{bmatrix}^T \in \mathbb{R}^3$ be the state vector of a nonlinear system $(\mathcal{S})$ whose output dynamic $y$ is simulated in MATLAB Simulink by the following equations:

$$(\mathcal{S}) : \begin{cases} \dot{x}_1 = -x_1 - e^{x_2} \sin(x_3) - x_2 \sqrt{|u + d|}, \\ \dot{x}_2 = -x_2 e^{x_1} - \sinh(u + d), \\ \dot{x}_3 = -2 \tan x_1 + x_2 x_3 + (u + d)^2, \\ y = x_1 x_2 x_3. \end{cases} \tag{7}$$

with $d$ an environmental phenomenon assumed to affect $u$ under the form of an additive sinusoidal disturbance defined by $d = 0.1 \exp^{-0.1t} \sin(0.2\pi t)$. The theoretical input $u$ of $(\mathcal{S})$ is a sequence of two opposite step inputs occurring at 2s and 16s respectively, as shown in Fig. 2. The linear model $(\mathcal{M})$ is assumed to be a first order
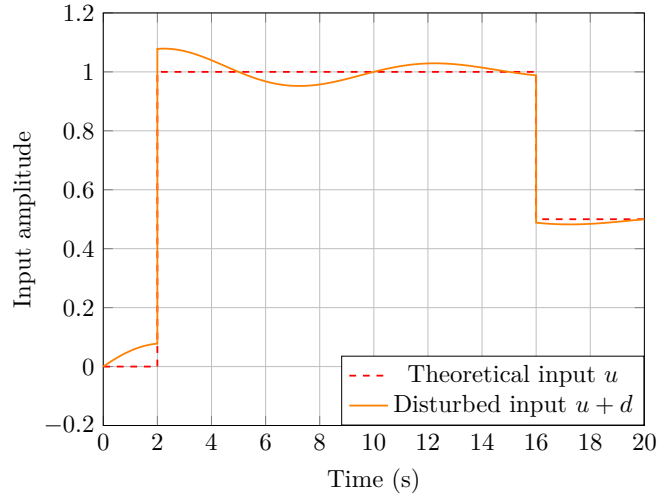


Figure 2: Comparison between theoretical input $u$ and the effective input of $(\mathcal{S})$ considering $d$.

model whose state vector is $X_m \in \mathbb{R}$. The following state-space representation defines its behavior:

$$(\mathcal{M}) : \begin{cases} \dot{X}_m = -X_m + 0.8u, \\ y_m = X_m. \end{cases} \tag{8}$$

As required by Theorem 1, the system $(\mathcal{S})$ and the model $(\mathcal{M})$ have the same initial conditions on their output $(y = y_m = 0)$, and are both fed by the theoretical input $u$. Fig. 3a illustrates the dynamics of $y$ and $y_m$. Since $(\mathcal{M})$ is clearly different from the nonlinear system $(\mathcal{S})$ and does not take the external disturbance into account, the discrepancy is large. Nevertheless, based on Theorem 1, the approximate model $(\mathcal{M})$ can be corrected to match $(\mathcal{S})$ by adding the virtual input $\mathcal{I}$ plotted in Fig. 3b,
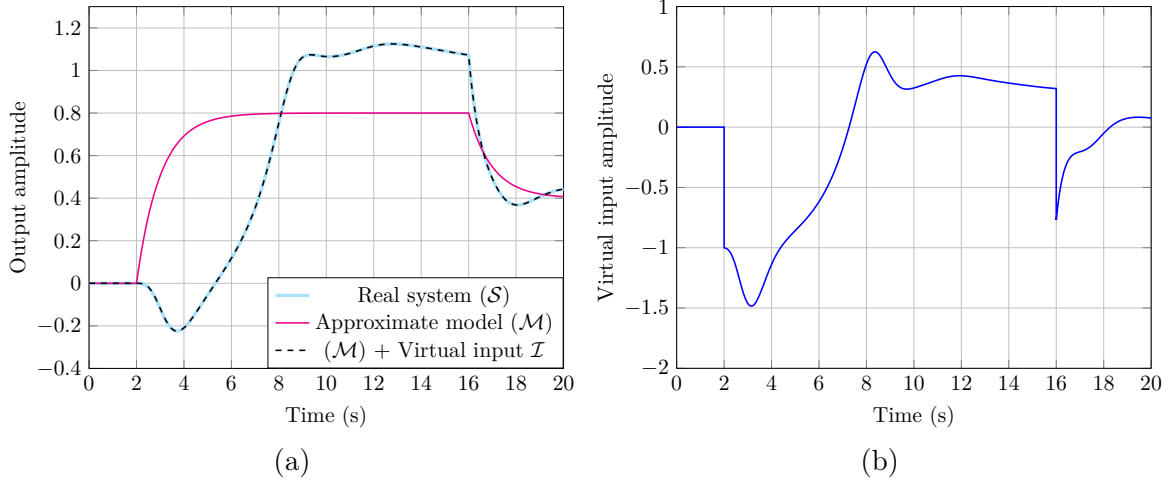
Figure 3: (a) Comparison between nonlinear system $(\mathcal{S})$ dynamics and outputs of the identified and equivalent models. (b) Plot of the associated virtual input $\mathcal{I}$.

to the step input $u$. The dashed curve in Fig. 3a represents the equivalent model of the nonlinear system $(\mathcal{S})$ given by the following state-space representation:

$$(\mathcal{S}) \Leftrightarrow \begin{cases} \dot{X} = -X + 0.8(u + \mathcal{I}), \\ y = X \end{cases} \tag{9}$$

In this short example, the input $u$ and the output $y$ of $(\mathcal{S})$ are directly available in the Simulink model. The first derivative $\dot{y}$ is computed using the analytical expression $\dot{x}_1 x_2 x_3 + x_1 \dot{x}_2 x_3 + x_1 x_2 \dot{x}_3$ determined from Equation (7). The theoretical virtual input required to correct the behavior of $(\mathcal{M})$ is deduced from Equation (9), which gives:

$$\mathcal{I} = \frac{1}{0.8}\left[\dot{x}_1 x_2 x_3 + x_1 \dot{x}_2 x_3 + x_1 x_2 \dot{x}_3 + y - 0.8u\right]. \tag{10}$$

The previous equation illustrates that the value of $\mathcal{I}$ is causally linked to the input-output behavior of $(\mathcal{S})$ given by $u$, $y$, its internal states $x_1$, $x_2$, $x_3$ and their derivatives.

## 2.2 Step two: Virtual input shaping

As a reminder, the objective is to estimate the quantities in $Q$ amongst all the disturbances $d \in \mathbb{R}^\delta$ that affect the system $(\mathcal{S})$. The uncertainty associated to this estimate must also be determined. As the equation for the nonlinear dynamics of $(\mathcal{S})$ is not well known, its equivalent model is thus considered since both have the same input-output behavior. The discrepancy between the behavior of the linear model $(\mathcal{M})$ and $(\mathcal{S})$ corresponds to the virtual input $\mathcal{I}$, which includes all dynamics not described by $(\mathcal{M})$. This means that the virtual input $\mathcal{I}$ must be shaped, or structured, in order to distinguish the information of interest. All the quantities of interest which constitute the relevant information to be estimated, are present in the vector $Q$:

$$Q(t) = \begin{bmatrix} q_1 & \cdots & q_\lambda \end{bmatrix}^T \in \mathbb{R}^\lambda. \tag{11}$$

The disturbing phenomena present in $d$, that are different from $Q$ and that can be quantified by measurements, are called measurement biases and are inventoried in the vector $D$:

$$D(t) = \begin{bmatrix} d_1 & \dots & d_\nu \end{bmatrix}^T \in \mathbb{R}^\nu. \tag{12}$$

The dimension of the vectors $Q$ and $D$ necessarily satisfies $\lambda + \nu \leq \delta$. The quantities gathered in these two vectors corresponds to physical phenomena that change the dynamical behavior of $(\mathcal{S})$. According to its definition (3), the model $(\mathcal{M})$ does not consider the input disturbances $d$. Thus, the dynamics associated with $Q$ and $D$ are necessarily included in the virtual input $\mathcal{I}$. A measurement model must be introduced to describe the dynamics of the quantities of interest and the measurement biases in $\mathcal{I}$, so that they become an input additive to the physical input $u$ of $(\mathcal{M})$. The modeled dynamics of the virtual input is described by introducing a shaping model $h : \mathbb{R}^\lambda \times \mathbb{R}^\nu \to \mathbb{R}$ that verifies:

$$\mathcal{I}(t) = h(Q(t), D(t)) + \varepsilon(t). \tag{13}$$

Indeed, $h$ is an incomplete representation of the physics whereas $\mathcal{I}$ corresponds to the actual discrepancy between the dynamics of the model $(\mathcal{M})$ and the system $(\mathcal{S})$. This means that $h$ is an approximation of $\mathcal{I}$ and that according to the theorem of equivalent representation, a Residual Shaping Error (RSE) noted $\varepsilon$ remains. Thus, the better the consistency of the shaping model $h$ used, the smaller the absolute value of the RSE. This step corresponds to the blue overlay in Fig. 1.

## 2.3 Step three: Estimation of the virtual input

In Fig. 1, the uncertain nonlinear system $(\mathcal{S})$ and its equivalent representation (5) are both represented in the red overlay. According to the principle of equivalent representation, the quantities that can be used to estimate the virtual input $\mathcal{I}$ with an observer are the matrices of the linear model $(\mathcal{M})$, and the input-output signals $u$ and $y$ of the system $(\mathcal{S})$. Since the model $(\mathcal{M})$ is chosen, its matrices $A$, $B$ and $C$ are known and thus certain. However, the signals $u$ and $y$ are unknown, so only the available values $u^c$ and $y^m$ can be used. Consequently, the uncertainty associated with the estimate of the virtual input solely comes from the values of $u^c$ and $y^m$ when they are not strictly equal to $u$ and $y$. Indeed, these differences represent a source of uncertainty which is due to drift phenomena, electronic noise or D/A and A/D conversion errors, and which will then deteriorate the estimation of $\mathcal{I}$. If this uncertainty is assumed to be unknown-but-bounded, intervals $[u^c]$ and $[y^m]$ in which the actual values of $u$ and $y$ are expected, can be defined. Otherwise, random variables and probability density functions can be introduced to account for the uncertainty associated with $u^c$ and $y^m$ if a probabilistic approach is appropriate. Whatever approach is chosen, calibrated instruments must be used to determine the uncertainty of the observer inputs, in order to guarantee the metrological traceability of the experiment. The methodology proposed here refers to existing observation techniques, without presenting any innovation in this field. Therefore, any linear observer able to provide

an interval $[\hat{\mathcal{I}}]$ that verifies $\mathcal{I} \in [\hat{\mathcal{I}}]$ on the basis of $[u^c]$, $[y^m]$ and a linear model similar to $(\mathcal{M})$, is a potential candidate. This first calculation stage corresponds to the green overlay in Fig. 1. In the literature, interval observers [36], set-valued observers [37], and set membership estimators [38] are classical approaches potentially usable if uncertainty is assumed to be unknown-but-bounded. Otherwise, when uncertainties are represented by probabilistic distributions, a Bayesian statistical inference can be used inside the observer to propagate each uncertainty onto the system state that must include the virtual input as a state component [39].

## 2.4   Step four: Uncertainty propagation

The proposed approach aims to define intervals for the quantities of interest $q_1, \dots, q_\lambda$ present in $Q$, based on the shaping model $h$, an estimated interval $[\hat{\mathcal{I}}]$ and the measurement biases gathered in $D$. The biases can be measured directly on the experimental device with a metrological quality that enables an uncertainty interval $[D^m]$ to be defined. Table 1 summarizes the notations introduced for this methodology and the corresponding meanings. Using (13), the objective is represented conceptually by finding estimated intervals $[\hat{Q}]$ based on $[\hat{\mathcal{I}}]$ and $[D^m]$ such that $h([\hat{Q}], [D^m]) \equiv [\hat{\mathcal{I}}]$. This second calculation stage is represented by the yellow overlay in Fig. 1. The RSE $\varepsilon$ is necessarily neglected for calculation purposes, as it is unknown in practice. This problem is similar to an inverse problem, extended in the following to the framework of interval analysis where efficient solving tools are available.

| Quantity | Signification |
|---|---|
| $Q$ | Multidimensional vector gathering the quantities of interest |
| $[\hat{Q}]$ | Symbolic notation representing the uncertainty associated with the estimated quantities of interest $\hat{Q}$ |
| $D$ | Multidimensional vector gathering the known measurement biases |
| $[D^m]$ | Uncertainty associated with the measured value $D^m$ of $D$ |
| $[u^c]$ | Uncertainty associated with the known numerical command $u^c$ |
| $[y^m]$ | Uncertainty associated with the measured output $y^m$ |
| $[\hat{\mathcal{I}}]$ | Uncertainty associated with the estimated virtual input $\hat{\mathcal{I}}$ |
| $\varepsilon$ | Unknown residual shaping error (RSE) of the virtual input $\mathcal{I}$ |

Table 1: Summary of the notations used in the proposed methodology.

### 2.4.1   Interval analysis : useful concepts

This section provides some basic elements of interval analysis useful for the understanding of this article. More information can be found for instance in [40, 41]. An interval $[x]$ is a closed and connected subset of $\mathbb{R}$:

$$[x] = [\underline{x}, \overline{x}] = \{x \in \mathbb{R} \mid \underline{x} \leq x \leq \overline{x}\}. \tag{14}$$

The real numbers $\underline{x}$ and $\overline{x}$ are respectively the lower and upper bounds of $[x]$. The width $w$ of an interval $[x]$ is defined by $w([x]) = \overline{x} - \underline{x}$. The set of real intervals is denoted by $\mathbb{IR}$. An interval vector of $\mathbb{IR}^n$, also called a box, is the Cartesian product of $n$ intervals of $\mathbb{IR}$:

$$[\mathbf{x}] = [\underline{x}_1, \overline{x}_1] \times \ldots \times [\underline{x}_n, \overline{x}_n] = [x_1] \times \ldots \times [x_n]. \tag{15}$$

As for intervals, the lower and upper bounds of a box can be defined as $\underline{\mathbf{x}} = (\underline{x}_1, \ldots, \underline{x}_n)^T$ and $\overline{\mathbf{x}} = (\overline{x}_1, \ldots, \overline{x}_n)^T$. The width $w([\mathbf{x}])$ of a $[\mathbf{x}]$ box is equal to the width of its widest component. Arithmetic operations $\circ \in \{+, -, ., /\}$ between real numbers have been extended to intervals:

$$[x] \circ [y] = \{x \circ y \mid x \in [x], y \in [y]\}. \tag{16}$$

Their specific calculation is done according to the form given in [40].

Let $\mathbf{f}$, be a function from $\mathbb{R}^p$ to $\mathbb{R}^q$. The image set of $\mathbf{f}$ can be enclosed by a box in a guaranteed way. Therefore, the set-valued function $[\mathbf{f}] : \mathbb{IR}^p \to \mathbb{IR}^q$ is an inclusion function of $\mathbf{f}$ if it ensures:

$$\forall \, [\mathbf{x}] \in \mathbb{IR}^p, \; \mathbf{f}([\mathbf{x}]) \subset [\mathbf{f}]([\mathbf{x}]). \tag{17}$$

It is important to note $\mathbf{f}$ is a vector-valued function whose domain is $\mathbb{R}^p$, but when applied to intervals, $\mathbf{f}([\mathbf{x}])$ refers to the image of $[\mathbf{x}]$ by $\mathbf{f}$ in a set sense. According to the previous definition, a given function $\mathbf{f}$ can have several inclusion functions. If the expression of $\mathbf{f}$ is explicitly known, replacing all occurrences of the input variables by their corresponding intervals, and all elementary operators and functions by their interval extensions, is an easy, but not necessarily optimal, way to find an inclusion function. The resulting interval function is said to be the natural inclusion function of $\mathbf{f}$.

### 2.4.2   Set inversion problem

To determine $[\hat{Q}]$, the proposed method propagates the uncertainty associated to $\hat{\mathcal{I}}$, computed at each discrete $k$-th time instant through the shaping model $h$. An interval is assigned to each component of $D$, which takes into account at least the noise of the sensors used to estimate them. The bias vector $D$ is therefore replaced by the box $[\mathbf{d}_k^m]$:

$$[\mathbf{d}_k^m] = [d_{1,k}^m] \times \ldots \times [d_{\nu,k}^m] \in \mathbb{IR}^\nu \tag{18}$$

which includes the feasible values of the measurement biases. If the physical parameters involved in the shaping model $h$ are uncertain, intervals can also be introduced and assigned to them. From a set-membership viewpoint, this inversion problem consists in characterizing in a guaranteed way, the solution set $\mathbb{S}_k$ defined for a given $[\mathbf{d}_k^m]$ by:

$$\mathbb{S}_k = \left\{ Q \in \mathbb{R}^\lambda \mid \exists \, \mathbf{d} \in [\mathbf{d}_k^m], \ h(Q, \mathbf{d}) \in [\hat{\mathcal{I}}_k] \right\}. \tag{19}$$

If unfeasible values of the quantities present in $Q$ are known, additional relations can be introduced to remove them when solving the set inversion problem. The $r^{\text{th}}$ relation of a set of $\rho$ relations can be defined by a function $\pi_r : \mathbb{R}^\lambda \to \mathbb{R}$ associated to an interval $[c_r]_k$ in which the relation is valid. The computation of $\pi_r$ takes a candidate $Q$ as an input and must satisfy the following condition:

$$\pi_r(Q) \in [c_r]_k. \tag{20}$$

Adding relations may sometimes help when finding a box with non-infinite bounds is impossible due to the dimension of $Q$ and the expression of the shaping model $h$. Other shaping models involving these quantities of interest are also suitable for supplementing Equation (19). The application example in the next part illustrates this point using virtual inputs provided by complementary systems. Therefore, the previous solution set $\mathbb{S}_k$ can be turned into

$$\mathbb{S}_k = \left\{ Q \in \mathbb{R}^\lambda \ \middle| \ \begin{array}{l} \exists \, \mathbf{d} \in [\mathbf{d}_k^m], \ h(Q, \mathbf{d}) \in [\hat{\mathcal{I}}_k], \\ \pi_r(Q) \in [c_r]_k, \ \forall r \in [1, \rho]. \end{array} \right\}. \tag{21}$$

The estimation process aims at finding a box $[\mathbf{q}_k] \in \mathbb{IR}^\lambda$ that gathers an uncertainty interval for each quantity of interest such that

$$\mathbb{S}_k \subset [\mathbf{q}_k], \text{ with } [\mathbf{q}_k] = [q_{1,k}] \times \ldots \times [q_{\lambda,k}]. \tag{22}$$

Depending on the physical nature of the quantities to be estimated, several potentially complex shaping models may be introduced. Robust algorithms able to solve such an inverse problem have been developed using the framework of interval analysis. These algorithms are suitable for a large class of problem involving complex shaping models with serious nonlinearities. The Set Inverter Via Interval Analysis algorithm (SIVIA) [42] is an iterative bisection process based on subpavings that determines an accurate and guaranteed representation of the solution set, as long as an inclusion function is provided. An improved version of the SIVIA algorithm, called SIVIAP, has been developed by introducing constraint propagation on intervals [43]. This improved version is used in the following application example to compute the box $[\mathbf{q}_k]$, which regroups the uncertainty associated with the unknown accelerations to be estimated.

## 2.5   Procedure summary

This section summarizes the procedure to be followed to correctly implement the proposed methodology for calculating uncertainty.

13

1. Define the input $u$ and the output $y$ of the dynamical system $(\mathcal{S})$ to be studied;

2. Determine the three $p$-order matrices $A$, $B$ and $C$ of a linear model $(\mathcal{M})$ whose input is $u$;

3. Write the equivalent representation of $(\mathcal{S})$ based on $u$, $y$, $(\mathcal{M})$ and a virtual input $\mathcal{I}$ as in Equation (5);

4. Gather the quantities of interest to be estimated in a vector $Q$, and the known measurement biases in a vector $D$ ;

5. Find a shaping model $h$ as a function of $Q$ and $D$ that models the dynamics of the virtual input $\mathcal{I}$;

6. Write the shaping expression of the virtual input $\mathcal{I}$ introducing the RSE $\varepsilon$, as in Equation (13);

7. Characterize the uncertainty $[\mathrm{u}^c]$ and $[\mathrm{y}^m]$ respectively related to the signals $u$ and $y$, considering the known command $\mathrm{u}^c$ of $(\mathcal{S})$, and the measured value $\mathrm{y}^m$ of its output;

8. Implement a linear observer able to provide an estimated interval $[\hat{\mathcal{I}}]$ on the basis of $(\mathcal{M})$, $[\mathrm{u}^c]$ and $[\mathrm{y}^m]$;

9. Determine the uncertainty $[\mathrm{D}^m]$ associated with the measured value $\mathrm{D}^m$ of $D$;

10. Extend the shaping model $h$ to the framework of interval analysis, considering the box $[\mathbf{d}_k^m]$ for $[\mathrm{D}^m]$, and intervals for the uncertain parameters involved;

11. Solve the set inversion problem defined by the Equation (21), whose solution corresponds to the uncertainty $[\hat{Q}]$ associated with the estimated quantities of interest $\hat{Q}$.

# 3 Application example: Estimation of unknown accelerations

In this second part, the methodology for the estimation of specific unknown inputs is applied on the triaxial accelerometer dedicated to the microforce balance under development. This accelerometer actually consists of three similar coupled uniaxial accelerometers, arranged to operate in each direction of space (see Fig. 4a). For this reason, the following case study mainly focuses on the $x$-axis. The sensitive part of $x$-accelerometer is a micromachined piece of aluminum with two $300\mu m$-diameter rods, which has in its center a $1mm$-high and $1mm$-diameter cylindrical magnet. This magnetic pendulum is maintained in contact upwards with the frame thanks to a permanent magnet, which prevents it from falling (see Fig. 4b). Like a swing, the
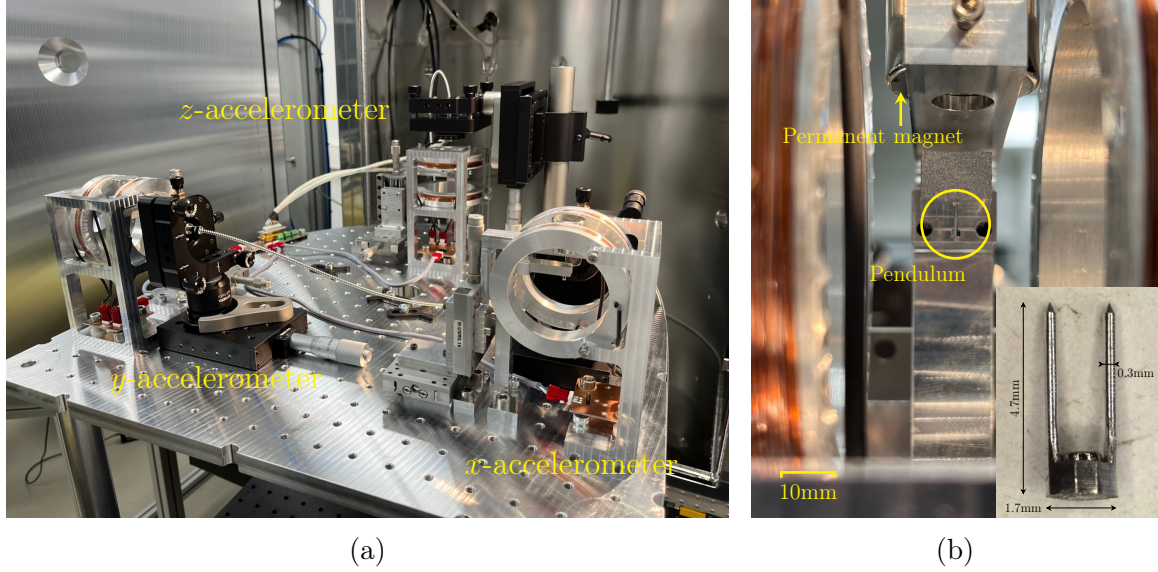
Figure 4: (a) Global view of the complete triaxial accelerometer. (b) Picture of a pendulum attracted by a permanent magnet.

pendulum oscillates when the frame is moving under the effect of disturbing vibrations. According to the method described in Part 2, the $x$-accelerometer is considered as a nonlinear uncertain system ($\mathcal{S}^x$) disturbed by several unknown inputs, including residual ground vibrations. The orientation of the pendulum is measured using a displacement interferometer and corresponds to the output of ($\mathcal{S}^x$). Then, Helmholtz coils are placed around the pendulum to generate an electromagnetic torque able to change its orientation. In this way, open-loop characterization tests can be carried out, and closed-loop control can also be considered. The current $i^x$ flowing through the coils is chosen as the control input of ($\mathcal{S}^x$). Although only open-loop studies are presented here, the pendulum modeling includes the control input so that it can be referenced in future closed-loop works. The aim of this application example is to illustrate each step of the methodology using MATLAB Simulink R2020b. Numerical simulations are developed as they make possible the study of the RSEs, and also enable estimated quantities to be compared with the corresponding simulated unknown inputs that are not accessible in practice.

## 3.1 Simulation of the disturbed $x$-accelerometer

Before moving on to the first step of the methodology, the mechanical modeling used to simulate the $x$-accelerometer is presented. As shown in Fig. 5, the $x$-accelerometer is placed in a non-inertial frame $R_t = (O_t, \vec{x}_t, \vec{y}_t, \vec{z}_t)$ linked to the vibration isolation table. The tabletop normal vector is collinear with $\vec{z}_t$. The system is continuously disturbed by accelerations defined in $R_t$ by $\vec{a}_{ie} = [\ddot{x}_\alpha, \ \ddot{y}_\alpha, \ \ddot{z}_\alpha]^T$. These accelerations are the consequences of the unknown displacements $\vec{u}_d = (x_d, y_d, z_d)_{R_t}$ of the tabletop with respect to the inertial frame $R_g = (O_g, \vec{x}_g, \vec{y}_g, \vec{z}_g)$, linked to the laboratory. The tabletop freely rotates in space, due to pneumatic active damping, but the angular
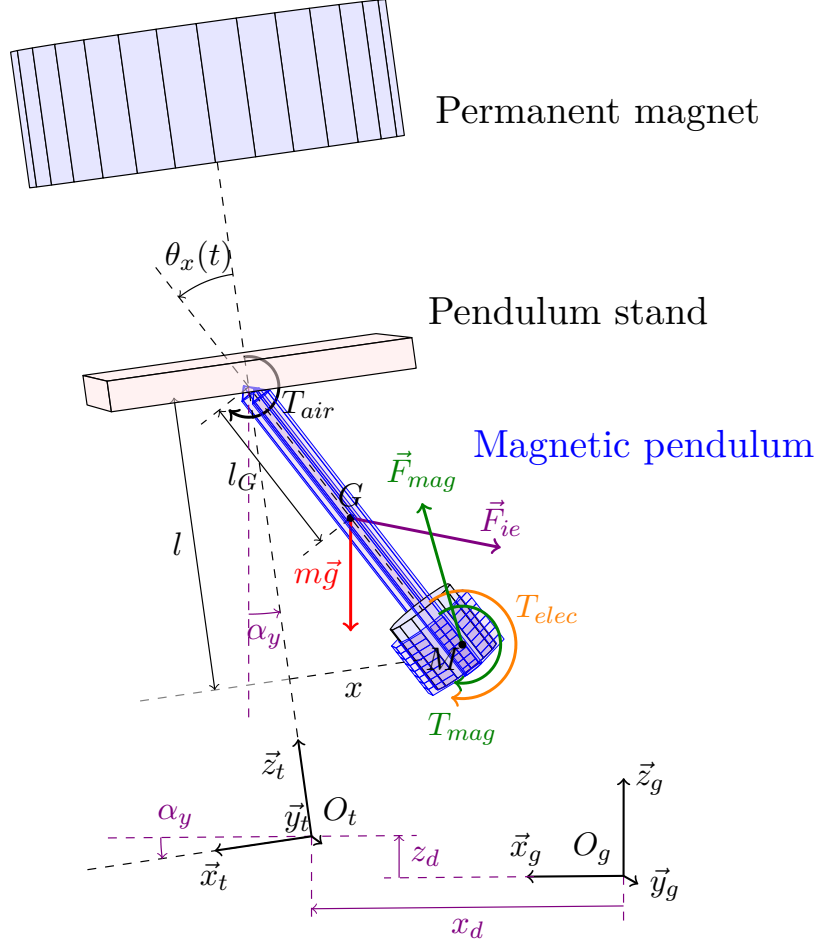
Figure 5: Schematic of the pendulum used to define the mechanical equations of its dynamics. The value of $\alpha_x$ is set to zero on the drawing.

velocities are low, so the effects are supposed negligible compared to the other dynamics. Rotational inertial effects are therefore neglected, and fictitious forces $\vec{F}_{ie}$, only due to straight accelerations, are introduced to describe the dynamics of the pendulum. However, these tabletop rotations, considered static, still modify the tilt of the pendulum as the direction of gravity is fixed. Since the current setup is only instrumented for pitch and roll measurement, two angles, $\alpha_x$ and $\alpha_y$, are introduced to describe the tilts around $\vec{y}_t$ and $\vec{x}_t$ respectively. The weight $\vec{W}$ of the pendulum and $\vec{F}_{ie}$ can be expressed as follows:

$$\vec{W} = -mg \begin{bmatrix} -\sin(\alpha_y) \\ \cos(\alpha_y)\sin(\alpha_x) \\ \cos(\alpha_y)\cos(\alpha_x) \end{bmatrix}_{R_t} , \vec{F}_{ie} = -m \begin{bmatrix} \ddot{x}_\alpha \\ \ddot{y}_\alpha \\ \ddot{z}_\alpha \end{bmatrix}_{R_t} \tag{23}$$

with $m$ the mass of the pendulum. As the pendulum is an oscillating system, external forces are represented by torques. $T_{eq}$ is assumed to be the equivalent magnetic torque created by the carrier magnet, $T_{air}$ the resistance torque induced by air friction, and

$T_{elec}$ the electromagnetic torque induced by the actuation system:

$$T_{eq} = \big[\vec{M}(\vec{F}_{mag}) + T_{mag}\big]\vec{y}_t = -K_m^x\theta_x\vec{y}_t, \tag{24}$$

$$T_{air} = -K_v^x\dot{\theta}_x\vec{y}_t, \tag{25}$$

$$T_{elec} = -K_b^x i^x \vec{y}_t \tag{26}$$

in which $K_m^x$ is the equivalent proportional gain, which describes the magnetic behavior of the pendulum immersed in the permanent magnetic field around its pseudo-equilibrium position, $K_v^x$ the air friction coefficient which is non-null outside the vacuum chamber, and $K_b^x$ the actuation gain related to the Helmholtz coil arrangement. The resulting torque balance is stated in $R_t$ as follows:

$$
\begin{aligned}
J\ddot{\theta}_x = & - K_b^x i^x - K_v^x \dot{\theta}_x - K_m^x \theta_x \\
& - mgl_G\big[\cos(\theta_x)\sin(\alpha_y) + \sin(\theta_x)\cos(\alpha_x)\cos(\alpha_y)\big] \\
& + ml_G\big[\ddot{x}_\alpha\cos(\theta_x) - \ddot{z}_\alpha\sin(\theta_x)\big].
\end{aligned} \tag{27}
$$

As the system is observed through a displacement sensor, a change of variable from $\theta_x$ to $x$ has to be implemented to correctly describe the dynamics captured:

$$x = -l\tan(\theta_x), \tag{28}$$

By expressing the analytical first and second derivatives of $\theta_x$ in terms of $x$ using the Equation (28), the nonlinear torque balance (27) can be turned into:

$$
\begin{aligned}
\ddot{x} = & \frac{l(1 + (\frac{x}{l})^2)}{J}\Bigg[mgl_G\big[\text{c}(\theta_x)\text{s}(\alpha_y) + \text{s}(\theta_x)\text{c}(\alpha_y)\text{c}(\alpha_x)\big] - ml_G\big[\ddot{x}_\alpha\text{c}(\theta_x) - \ddot{z}_\alpha\text{s}(\theta_x)\big] \\
& + K_m^x\theta_x - K_v^x\frac{\dot{x}}{l(1 + (\frac{x}{l})^2)} + K_b^x i^x\Bigg] + \frac{2\dot{x}^2 x}{l^2(1 + (\frac{x}{l})^2)}, \text{ in which } \theta_x = \text{atan}\Big(-\frac{x}{l}\Big),
\end{aligned} \tag{29}
$$

with $J$ the momentum of inertia of the pendulum, $l_G$ the position of its center of gravity and $l$ the position of the laser sport on the pendulum. Similar modeling is carried out for the other axes. Although not detailed here, the nonlinear equations obtained are used to simulate the complete triaxial accelerometer. The unknown disturbing accelerations $\vec{a}_{ie}$ to be estimated, and the tilt angles $\vec{\alpha}$ are modeled by band-limited white noise with noise power set respectively to $1 \times 10^{-7}$ m$^2$/s$^4$/Hz and $2\times10^{-9}$ rad$^2$/Hz in order to reproduce simulation conditions close to the experimental ones. Two cascaded first-order low-pass filters with a cutoff frequency of $f_c = 2$ Hz are added to simulate the filtering behavior of the vibration isolation system of the table. The variance $R$ of the interferometer measurement noise is set to $6.25 \times 10^{-20}$ m$^2$. The parameters involved in (29) are either identified on the actual experimental device, measured, or taken from CAD designs in order to obtain reliable simulation results that are close to the physics of the experiment. Table 2 makes an inventory of the values of the parameters used for the simulation. The open-loop output of the disturbed $x$-accelerometer is shown in Fig. 6.

| Parameter | Numerical value |
|-----------|-----------------|
| $g$ | $9.807$ m/s$^2$ |
| $m$ | $9.136 \times 10^{-6}$ kg |
| $J$ | $1.427 \times 10^{-10}$ kg.m$^2$ |
| $l_G$ | $3.831 \times 10^{-3}$ m |
| $l$ | $4.2 \times 10^{-3}$ m |
| $K_m^x$ | $7.540 \times 10^{-6}$ N.m |
| $K_v^x$ | $1.340 \times 10^{-10}$ kg.m$^2$.s$^{-1}$ |
| $K_b^x$ | $1.729 \times 10^{-6}$ N.m/A |
| $K_m^y$ | $7.537 \times 10^{-6}$ N.m |
| $K_v^y$ | $6.496 \times 10^{-11}$ kg.m$^2$.s$^{-1}$ |
| $K_b^y$ | $1.668 \times 10^{-6}$ N.m/A |
| $K_m^z$ | $7.333 \times 10^{-6}$ N.m |
| $K_v^z$ | $5.270 \times 10^{-11}$ kg.m$^2$.s$^{-1}$ |
| $K_b^z$ | $1.684 \times 10^{-6}$ N.m/A |

Table 2: Numerical values of the parameters used to simulate the response of the complete accelerometer.
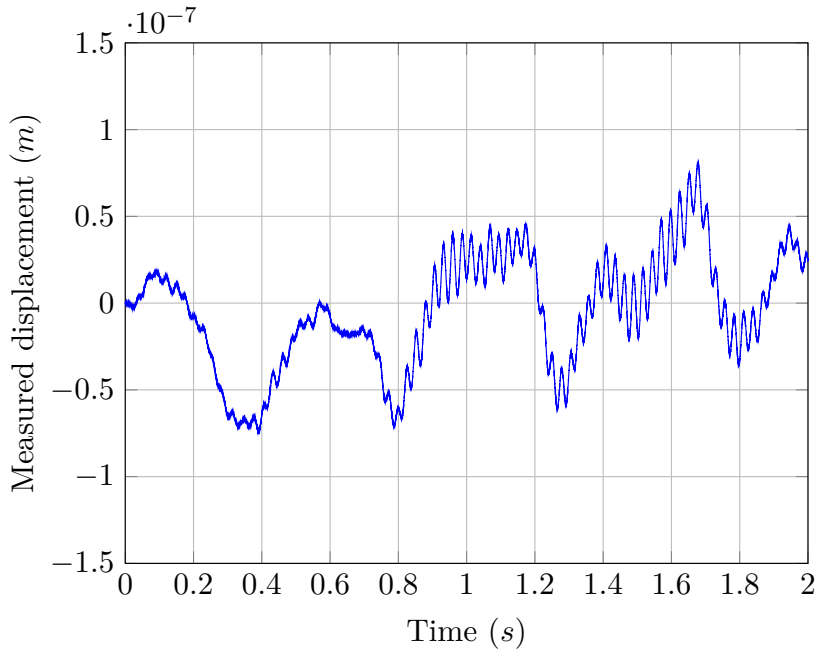


Figure 6: Simulation of the open-loop displacement of the $x$-pendulum excited by $\vec{a}_{ie}$ and $\vec{\alpha}$.

## 3.2 Step one: Equivalent representation

The first step of the method consists in determining a linear model that approximates the dynamical behavior of the system studied. To achieve this, the $x$-pendulum dynamics is identified on the real experiment by studying its zero-input response for

small displacements around its pseudo-equilibrium position. The captured displacement is consistent with a linear second-order response. Afterward, the static gain between the current injected into the coils and the displacement of the pendulum is determined by considering different steady state positions given for various constant input commands, which leads to the following linear transfer function:

$$H^x(s) = \frac{x(s)}{i^x(s)} = \frac{b^x}{s^2 + a_1^x s + a_0^x} = \frac{50.881}{s^2 + 0.974s + 55244}. \tag{30}$$

An equivalent representation can thus be determined on the basis of a fairly consistent linear model $(\mathcal{M}^x)$. In line with the theorem of equivalent representation invoked in 2.1, the true dynamics of the disturbed $x$-accelerometer is accurately described by the following state-space representation:

$$(\mathcal{S}^x) \Leftrightarrow \begin{cases} \dot{X} = \begin{bmatrix} 0 & 1 \\ -55244 & -0.974 \end{bmatrix} X + \begin{bmatrix} 0 \\ 50.881 \end{bmatrix} (i^x + \mathcal{I}^x), \\ x = \begin{bmatrix} 1 & 0 \end{bmatrix} X \end{cases} \tag{31}$$

in which $X = \begin{bmatrix} x & \dot{x} \end{bmatrix}^T \in \mathbb{R}^2$ is the state vector, and $\mathcal{I}^x$ the virtual input homogeneous to an electric current. The same procedure is repeated on $y$ and $z$ axes to determine the identified models $(\mathcal{M}^y)$ and $(\mathcal{M}^z)$, which give the following equivalent representations:

$$\begin{aligned} (\mathcal{S}^y) &\Leftrightarrow \begin{cases} \dot{Y} = \begin{bmatrix} 0 & 1 \\ -55222 & -0.455 \end{bmatrix} Y + \begin{bmatrix} 0 \\ 49.104 \end{bmatrix} (i^y + \mathcal{I}^y), \\ y = \begin{bmatrix} 1 & 0 \end{bmatrix} Y, \end{cases} \\ (\mathcal{S}^z) &\Leftrightarrow \begin{cases} \dot{Z} = \begin{bmatrix} 0 & 1 \\ -51385 & -0.369 \end{bmatrix} Z + \begin{bmatrix} 0 \\ 49.567 \end{bmatrix} (i^z + \mathcal{I}^z), \\ z = \begin{bmatrix} 1 & 0 \end{bmatrix} Z. \end{cases} \end{aligned} \tag{32}$$

## 3.3 Step two: Virtual input shaping

Regarding the $x$-accelerometer, all dynamics not described by the identified model $(\mathcal{M}^x)$ lie in the virtual input $\mathcal{I}^x$. A model must therefore be defined to structure the information contained in $\mathcal{I}^x$. The shaping of the virtual input must enable the estimation of the unknown accelerations of interest, taking into account known measurement biases. In this example, the accelerations $\vec{a}_{ie} = [\ddot{x}_\alpha, \ddot{y}_\alpha, \ddot{z}_\alpha]^T$ of the table plate have to be estimated, i.e. $Q = \vec{a}_{ie}$. However, when the plate is rotating with $\alpha_x$ or $\alpha_y$ different from zero, each part of the setup is tilted. As the direction of gravity does not change, the pendulum moves under the effect of its own weight. A displacement is measured and could be mistakenly considered as a consequence of $\vec{a}_{ie}$. Therefore, the angles $\alpha_x$ and $\alpha_y$ are gathered in a vector $\vec{\alpha}$ as measurement biases, i.e. $D = \vec{\alpha}$. As written in Section 2.2, shaping the virtual input consists in representing as best as possible its content under the form of a dynamical shaping model. The mechanical modeling of the accelerometer presented previously is used in

this third step to construct relatively consistent analytical expressions describing the dynamics of the virtual input. According to Equation (29), the nonlinear dynamics of the $x$-accelerometer is equivalent to:

$$\ddot{x} = \Delta_{\mathrm{NL}}^x(X, Q, D, i^x), \tag{33}$$

with $\Delta_{\mathrm{NL}}^x(X, Q, D, i^x)$ a nonlinear function defined by:

$$\Delta_{\mathrm{NL}}^x(X, Q, D, i^x) = \frac{2\dot{x}^2 x}{l^2(1 + (\frac{x}{l})^2)} - \frac{l(1 + (\frac{x}{l})^2)}{J}\left[ ml_G\Big(\ddot{x}_\alpha\mathrm{c}(\theta_x) - \ddot{z}_\alpha\mathrm{s}(\theta_x)\right.$$

$$\left. - g\big[\mathrm{c}(\theta_x)\mathrm{s}(\alpha_y) + \mathrm{s}(\theta_x)\mathrm{c}(\alpha_y)\mathrm{c}(\alpha_x)\big]\Big) - K_m^x\theta_x - K_b^x i^x \right] - \frac{K_v^x}{J}\dot{x}. \tag{34}$$

In practice, the actual disturbing inertial forces and table tilt angles acting on the triaxial accelerometer are small and generate rather linear oscillations. Consequently, the small displacement assumption ($x \ll l$) and the small-angle approximation are introduced to first simplify the nonlinear function $\Delta_{\mathrm{NL}}^x$, which leads to:

$$\ddot{x} = \Delta_{\mathrm{L}}^x(X, Q, D, i^x), \tag{35}$$

with $\Delta_{\mathrm{L}}^x(X, Q, D, i^x)$ a linearized function defined by:

$$\Delta_{\mathrm{L}}^x(X, Q, D, i^x) = \frac{lK_b^x}{J}i^x - l\frac{ml_G}{J}\left(\ddot{x}_\alpha + \ddot{z}_\alpha\frac{x}{l} - g\alpha_y\right) - \frac{K_v^x}{J}\dot{x} - \frac{mgl_G + K_m^x}{J}x. \tag{36}$$

The strategy to shape the virtual input emphasizes the distinction to be made between the certain model ($\mathcal{M}^x$) implemented to determine the equivalent representation, and the shaping model that will be used to propagate uncertainty. Therefore, the numerical values taken from Equation (30), are introduced artificially on both side of Equation (35) to bring out the model ($\mathcal{M}^x$):

$$\ddot{x} + a_1^x\dot{x} + a_0^x x = b^x i^x + \Delta_{\mathrm{L}}^x(X, Q, D, i^x) + a_1^x\dot{x} + a_0^x x - b^x i^x. \tag{37}$$

The shaping model has to make the virtual input $\mathcal{I}^x$ additive to $i^x$, like in the equivalent state-space representation (31). Therefore, the shaping model proposed, denoted by $h_{\mathrm{L}}^x$, is defined as:

$$h_{\mathrm{L}}^x(Q, D) = \frac{1}{b^x}\left[\Delta_{\mathrm{L}}^x(X, Q, D, i^x) + a_1^x\dot{x} + a_0^x x - b^x i^x\right]. \tag{38}$$

The exact pendulum dynamics is equivalently reproduced by adding $h_{\mathrm{L}}^x$ and the associated RSE $\varepsilon_{\mathrm{L}}^x$ on the control input $i^x$ of the identified model (30):

$$\ddot{x} + 0.974\dot{x} + 55244x = 50.881\left[i^x + h_{\mathrm{L}}^x(Q, D) + \varepsilon_{\mathrm{L}}^x\right]. \tag{39}$$

The RSE is homogeneous to an electric current that compensates for all modeling errors and represents all remaining unknown dynamics. The whole process is repeated

for the other axes and leads to the following virtual input shapes for the virtual inputs $\mathcal{I}^x$, $\mathcal{I}^y$ and $\mathcal{I}^z$ defined by Equations (31) and (32):

$$
\begin{cases}
\mathcal{I}^x = \dfrac{1}{b^x}\left[\Delta_{\mathrm{L}}^x(X, Q, D, i^x) + a_1^x \dot{y} + a_0^x x - b^x i^x\right] + \varepsilon_{\mathrm{L}}^x, \\[2mm]
\mathcal{I}^y = \dfrac{1}{b^y}\left[\Delta_{\mathrm{L}}^y(Y, Q, D, i^y) + a_1^y \dot{y} + a_0^y y - b^y i^y\right] + \varepsilon_{\mathrm{L}}^y, \\[2mm]
\mathcal{I}^z = \dfrac{1}{b^z}\left[\Delta_{\mathrm{L}}^z(Z, Q, D, i^z) + a_1^z \dot{z} + a_0^z z - b^z i^z\right] + \varepsilon_{\mathrm{L}}^z,
\end{cases}
\tag{40}
$$

with $Y = \begin{bmatrix} y & \dot{y} \end{bmatrix}^T$, $Z = \begin{bmatrix} z & \dot{z} \end{bmatrix}^T$ and $\varepsilon_{\mathrm{L}}^y$, $\varepsilon_{\mathrm{L}}^z$ the RSEs associated respectively with the shaping models of $y$ and $z$-measurement axes based on:

$$
\begin{aligned}
\Delta_{\mathrm{L}}^y(Y, Q, D, i^y) &= \frac{l K_b^y}{J} i^y - l\frac{m l_G}{J}\left(\ddot{y}_\alpha + \ddot{z}_\alpha \frac{y}{l} + g\alpha_x\right) - \frac{K_v^y}{J}\dot{y} - \frac{m g l_G + K_m^y}{J} y, \\
\Delta_{\mathrm{L}}^z(Z, Q, D, i^z) &= \frac{l K_b^z}{J} i^z - l\frac{m l_G}{J}\left(\ddot{z}_\alpha + \ddot{x}_\alpha \frac{z}{l} + g(1 - \frac{z}{l}\alpha_y)\right) - \frac{K_v^z}{J}\dot{z} - \frac{K_m^z}{J} z.
\end{aligned}
\tag{41}
$$

The linear shaping models corresponding to $h_{\mathrm{L}}^x$, $h_{\mathrm{L}}^y$ and $h_{\mathrm{L}}^z$ will then be used for uncertainty propagation.

The virtual input shaping is carried out using the mechanical modeling of the system, and thus only reflects an a priori state of knowledge, which is not perfect and may evolve in the future. The pendulum moment of inertia $J$ and the length $l_G$ of its center of gravity are supposed to be misidentified. Their value is assumed to be wrong to within 1% and are replaced by $J = 1.413 \times 10^{-10}$ kg.m$^2$ and $l_G = 3.869 \times 10^{-3}$ m in the three shaping models defined above, which will increase the value of the RSEs. The quantities present in $Q$ and $D$ are simulated and can therefore be used to plot the output of the shaping model $h_{\mathrm{L}}^x$ versus the theoretical value of $\mathcal{I}^x$ for small displacements with zero input current, corresponding to the accelerometer passive operating mode (see Fig. 7a). The shaping model is therefore consistent, but there remains a small difference between them corresponding to the RSE $\varepsilon_{\mathrm{L}}^x$ related to $h_{\mathrm{L}}^x$, illustrated in Fig. 7b. Such figures can only be plotted in simulation, as this is the only case where the theoretical value of the virtual input can be determined causally.

The nonlinear function $\Delta_{\mathrm{NL}}^x$ could have been used instead of $\Delta_{\mathrm{L}}^x$ to shape the virtual input. However, its linearized form is illustrated first in this article as it enables faster calculation of uncertainty, and no difference would have been observed for the small displacements considered, which do not exceed 0.1 $\mu$m. In Section 3.6, the accelerometer response is simulated with large excitation signals, in order to compare the consistency of the virtual input shaping based on the nonlinear function $\Delta_{\mathrm{NL}}$, and thus to highlight the suitability of this approach for dynamical systems described by a nonlinear model.
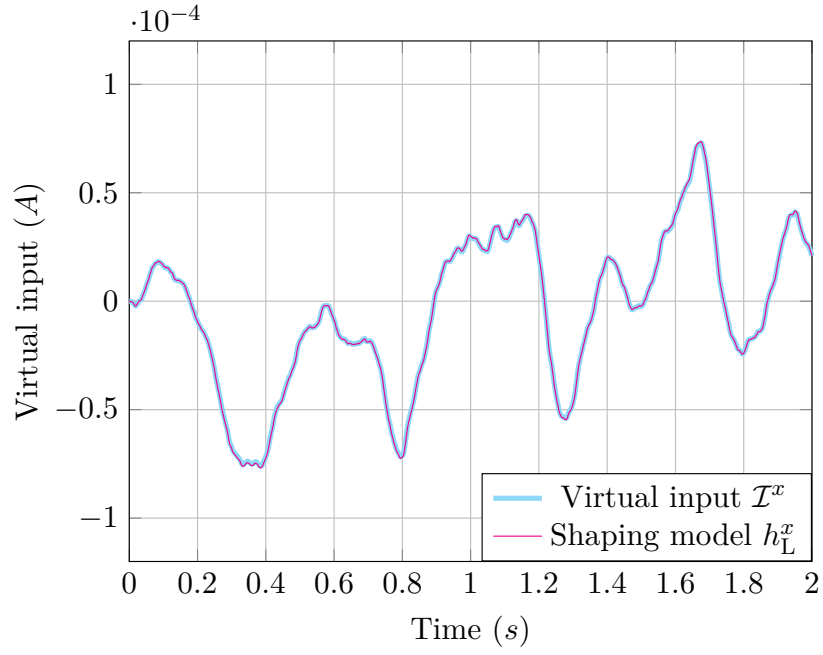
(a)
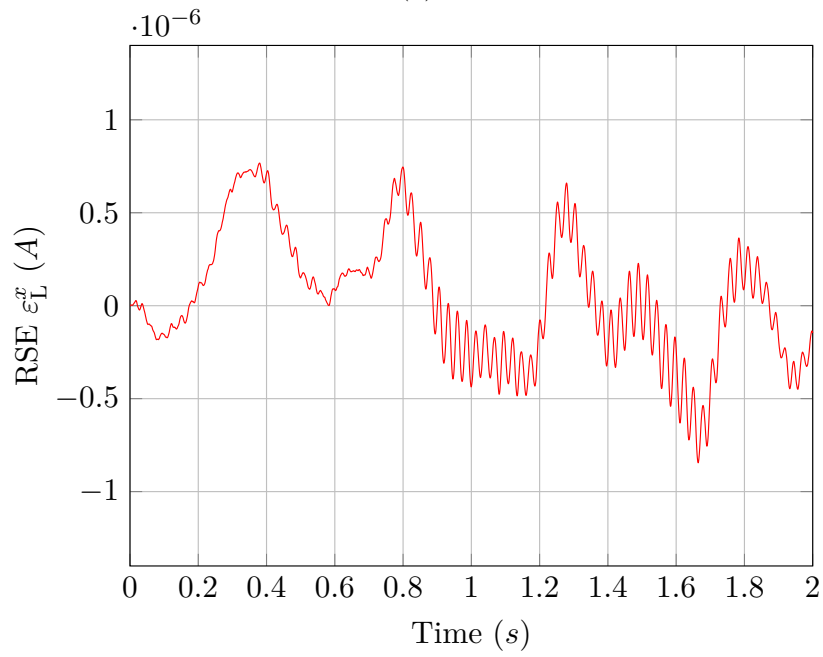


(b)

Figure 7: (a) Comparison of the shaping model $h_{\mathrm{L}}^x$ output and the theoretical virtual input value for small displacements with no input current. (b) Plot of the RSE $\varepsilon_{\mathrm{L}}^x$ associated to $h_{\mathrm{L}}^x$.

## 3.4 Step three: Estimation of the virtual input

The identified model $(\mathcal{M}^x)$ does not perfectly describe the behavior of the $x$-accelerometer $(\mathcal{S}^x)$ as it does not take into account nonlinearities, unknown accelerations $\vec{a}_{ie}$ and tilt angles $\vec{\alpha}$. An equivalent model has been determined to solve this problem by introducing the virtual input $\mathcal{I}^x$. In this application, a discrete time-varying linear Kalman Filter is used to observe the dynamics of $\mathcal{I}^x$ based on $(\mathcal{M}^x)$. Amokrane et al. already adapted it in [32] for this purpose by turning it into an Extended State Linear Kalman Filter (ES-LKF) of order 1 which belongs to the family of extended state observers (ESO) [33]. Nevertheless, only the uncertainty on the output was taken into account. A higher order (HO) version of the ES-LKF, that takes into account both input and output uncertainties, is considered here to be consistent with the proposed methodology. The extended state vector gathers the former states of the identified model $(\mathcal{M}^x)$ along with the virtual input $\mathcal{I}^x$ and its first derivative:

$$X^e = \begin{bmatrix} x & \dot{x} & \mathcal{I}^x & \dot{\mathcal{I}}^x \end{bmatrix}^T \in \mathbb{R}^4. \tag{42}$$

At time $t_k$, an estimated state vector $\hat{X}^e_k$ and the associated variance-covariance matrix of the observation error $\hat{P}_k$ are returned after each prediction-update step of the Kalman filter. The third component of $\hat{X}^e_k$ corresponds to the estimation of the virtual input, denoted by $\hat{\mathcal{I}}^x_k$. According to the definition of the covariance matrix, the third diagonal component of $\hat{P}_k$ thus gives the variance $\sigma^2_k$ of the observation error associated to $\hat{\mathcal{I}}^x_k$. According to the design of the HOES-LKF presented in B, this observation error and the associated variance depend on input and output signal uncertainties modeled by standard deviations, the sampling rate used and the power spectral density $w_{\mathrm{PSD}}$ of the white Gaussian noise used to model the second derivative of the virtual input $\mathcal{I}^x$ as an unpredictable signal. In the simulation, the parameter $w_{\mathrm{PSD}}$ is set to $4 \times 10^{-5}$ A$^2$/Hz. Although the input current uncertainty can be taken into account in a general case, it is set to zero since only the passive operating mode of the accelerometer is presented in this work. From there, the uncertainty interval associated to the estimate $\hat{\mathcal{I}}^x_k$ is defined at time $t_k$ by taking the $3\sigma$ rule:

$$\begin{bmatrix} \hat{\mathcal{I}}^x_k \end{bmatrix} \triangleq \begin{bmatrix} \hat{\mathcal{I}}^x_k - 3\sigma_k, & \hat{\mathcal{I}}^x_k + 3\sigma_k \end{bmatrix}. \tag{43}$$

This may not hold in some rare cases discussed in Section 4.2. The theoretical value of $\mathcal{I}^x$ and its estimate $\hat{\mathcal{I}}^x$ are both plotted in Fig. 8 with the associated $3\sigma$ bounds. Compared with the ES-LKF presented in [32], the HOES-LKF allows the virtual input to be estimated with less delay, but this comes at the cost of increased noise. Consequently, other observer structures can also be tested to find a better compromise for estimating the virtual input and its associated uncertainty. A HOES-LKF is implemented for each axis of the accelerometer, using the corresponding models $(\mathcal{M}^x)$, $(\mathcal{M}^y)$ and $(\mathcal{M}^z)$.

## 3.5 Step four: Uncertainty propagation

As previously mentioned, an implementation of the SIVIAP algorithm is used for the uncertainty propagation step. The next section introduces additional concepts of
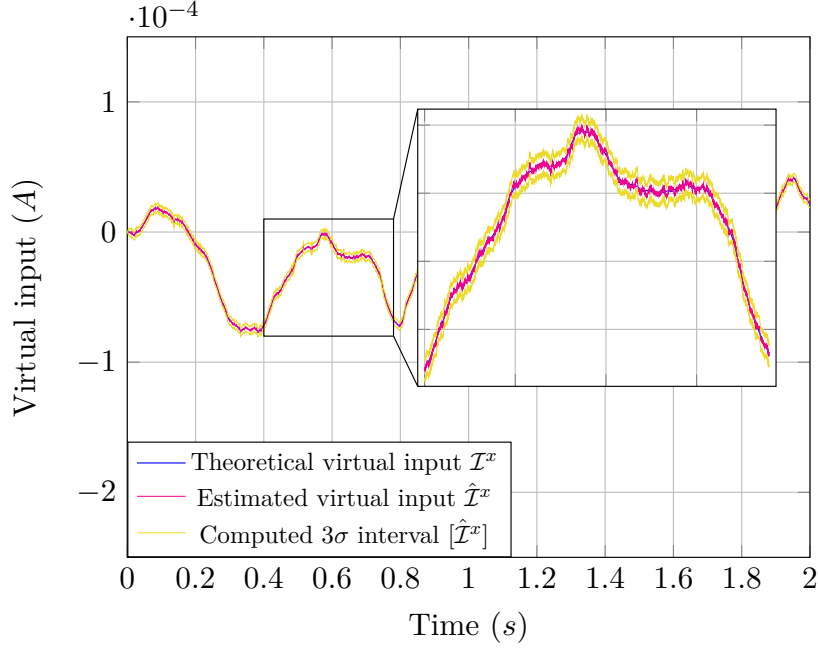
Figure 8: Plot of the theoretical virtual input $\mathcal{I}^x$, its estimated value $\hat{\mathcal{I}}^x$ and the $3\sigma$ bounds.

interval analysis and explains how the algorithm works.

### 3.5.1  Interval analysis : supplements

(a) *Inclusion tests:* an inclusion test is a boolean test applied to all elements of a box $[\mathbf{x}] \in \mathbb{IR}^n$ to determine whether they satisfy a given property. A property of particular interest to the SIVIAP algorithm is the inclusion of a box $[\mathbf{x}]$ in another set $\mathbb{X}$. The inclusion test $[t_{\mathbb{X}}]$ associated to $t_{\mathbb{X}}(\mathbf{x}) = (\mathbf{x} \in \mathbb{X})$ determines whether the elements of $[\mathbf{x}]$ are all included in $\mathbb{X}$ ($[t_{\mathbb{X}}]([\mathbf{x}]) = 1$), i.e. $[\mathbf{x}] \subset \mathbb{X}$, whether none of them are ($[t_{\mathbb{X}}]([\mathbf{x}]) = 0$), i.e. $[\mathbf{x}] \cap \mathbb{X} = \emptyset$, or whether only some of them are.

(b) *Contractor:* a contractor $\mathcal{C}$ is an operator able to reduce, or contract, a box by removing parts that do not satisfy a given constraint [44]. A constraint is an expression of the form $\gamma(\mathbf{x}) \in [\beta]$ in which $\gamma$ is a function from $\mathbb{R}^m$ to $\mathbb{R}^n$, and $[\beta]$ a box of $\mathbb{IR}^n$. The set associated with this constraint corresponds to the solution set $\mathbb{C} = \{\mathbf{x} \in \mathbb{R}^m \mid \gamma(\mathbf{x}) \in [\beta]\}$. Therefore, the contraction of a given box $[\mathbf{x}] \in \mathbb{IR}^m$ under this constraint returns a box $\mathcal{C}([\mathbf{x}]) \subset [\mathbf{x}]$ that satisfies $\mathcal{C}([\mathbf{x}]) \cap \mathbb{C} = [\mathbf{x}] \cap \mathbb{C}$. Finding such a box amounts to satisfying a constraint satisfaction problem (CSP). In the following SIVIAP implementation, the forward-backward contractor is used and tends to improve the algorithm efficiency. This contractor is based on the decomposition of a constraint into a sequence of primitive constraints to be evaluated forward and backward. For details of how it works, see [45].

24

(c) *SIVIAP algorithm:* this branch-and-bound algorithm is useful to estimate the solution set of an inverse problem without removing any solution from the search space. The solution set $\mathbb{S} \subset \mathbb{R}^m$ of an inverse problem is defined by:

$$\mathbb{S} = \left\{ \mathbf{x} \in [\mathbf{x}]_0 \mid \xi(\mathbf{x}) \in [\beta] \right\} = \xi^{-1}([\beta]) \cap [\mathbf{x}]_0, \tag{44}$$

with $[\mathbf{x}]_0 \in \mathbb{IR}^m$ the a priori initial search set, $\xi$ a function from $\mathbb{R}^m$ to $\mathbb{R}^n$, and $[\beta] \in \mathbb{IR}^n$ a known box. The recursive approach of SIVIAP uses bisections and the inclusion test $[t_{[\beta]}]$ associated to $t_{[\beta]}(\mathbf{x}) = (\xi(\mathbf{x}) \in [\beta])$, to provide a guaranteed enclosure of the solution set as follows:

$$\underline{\mathbb{S}} \subset \mathbb{S} \subset \overline{\mathbb{S}}, \tag{45}$$

with $\underline{\mathbb{S}}$ and $\overline{\mathbb{S}}$ respectively the inner and outer enclosures of $\mathbb{S}$. Let $[\mathbf{x}]$ be a box included in $[\mathbf{x}]_0$ and $[\xi]$ an inclusion function of $\xi$. If $[\xi]([\mathbf{x}]) \subset [\beta]$, $[\mathbf{x}]$ is said to be feasible and is assigned to $\underline{\mathbb{S}}$. If $[\xi]([\mathbf{x}]) \cap [\beta] = \emptyset$, $[\mathbf{x}]$ is unfeasible and is thus deleted. Otherwise, no conclusion can be drawn and $[\mathbf{x}]$ is said to be undetermined. In this case, $[\mathbf{x}]$ is bisected into two sub-boxes according to its largest width. The process is repeated recursively until the width of the generated sub-boxes reaches a user-specified precision threshold. At the end, the remaining undetermined boxes combined with $\underline{\mathbb{S}}$ constitute $\overline{\mathbb{S}}$. At each iteration, a contractor associated with the $\xi$ function is applied before proceeding with the inclusion tests. Adding this CSP improves the performance of the SIVIAP algorithm, since it reduces the number of bisections required to reach the precision threshold. The principle of the SIVIAP algorithm is summarized by the following procedure:

---

**Algorithm:** SIVIAP($[\mathbf{x}]_0$, $\mathcal{C}$, $[\mathbf{t}_{[\beta]}]$, $\eta$)

**Input:** $[\mathbf{x}]_0$, $\mathcal{C}$, $[\mathbf{t}_{[\beta]}]$, $\eta$
**Output:** $\underline{\mathbb{S}}$, $\overline{\mathbb{S}}$

$\mathcal{L} = \{[\mathbf{x}]_0\}$; $\underline{\mathbb{S}} = \emptyset$; $\overline{\mathbb{S}} = \emptyset$; *% initialization*
**while** $\mathcal{L} \neq \emptyset$ **do**
    Remove an element $[\mathbf{x}]$ from $\mathcal{L}$;
    $[\mathbf{x}] = \mathcal{C}([\mathbf{x}])$;
    **if** $[\mathbf{t}_{[\beta]}]([\mathbf{x}]) = 1$ **then**
        $\underline{\mathbb{S}} = \underline{\mathbb{S}} \cup [\mathbf{x}]$;
        $\overline{\mathbb{S}} = \overline{\mathbb{S}} \cup [\mathbf{x}]$;
    **else if** $[\mathbf{t}_{[\beta]}]([\mathbf{x}]) = 0$ **then**
        Delete $[\mathbf{x}]$;
    **else if** $w([\mathbf{x}]) \leq \eta$ **then**
        $\overline{\mathbb{S}} = \overline{\mathbb{S}} \cup [\mathbf{x}]$;
    **else**
        Bisect $[\mathbf{x}]$ into $[\mathbf{x}]_1$, $[\mathbf{x}]_2$ and store them in $\mathcal{L}$;
        SIVIAP($[\mathbf{x}]_1$, $\mathcal{C}$, $[\mathbf{t}_{[\beta]}]$, $\eta$);
        SIVIAP($[\mathbf{x}]_2$, $\mathcal{C}$, $[\mathbf{t}_{[\beta]}]$, $\eta$);
**end**

---

### 3.5.2 Uncertainty propagation

Given the terms in Equation (40), the intervals $[\hat{\mathcal{I}}^x]$, $[\hat{\mathcal{I}}^y]$, $[\hat{\mathcal{I}}^z]$ estimated by the HOES-LKFs are introduced instead of their theoretical value $\mathcal{I}^x$, $\mathcal{I}^y$ and $\mathcal{I}^z$. The displacements $x$, $y$, $z$ are replaced respectively by the intervals $[x]$, $[y]$, $[z]$ following the $3\sigma$ rule, which gives for instance $[x] = [x-3\sqrt{R},\ x+3\sqrt{R}]$ for the $x$-accelerometer, $R$ being the noise variance of the interferometer. In the same manner, uncertainty intervals are determined for the measurements $\alpha_x^m$ and $\alpha_y^m$ of the table tilts, with $R_\alpha = 10^{-10}$ rad$^2$ the noise variance of the measuring instrument used. The mass of the pendulum has been measured to an accuracy of 0.1 mg, so an interval $[m]$ is introduced for calculating the uncertainty. The position $l$ of the laser spot pointing at the pendulum is also replaced by an interval $[l]$ as it is not perfectly accurate in practice. Intervals centered around the erroneous value of parameters $J$ and $l_G$ are also introduced. The changes made to the values initially used to simulate the accelerometer are summarized in Table 3.

| Parameter | Interval value |
|---|---|
| $J$ (kg.m$^2$) | $[1.403 \times 10^{-10},\ 1.423 \times 10^{-10}]$ |
| $l_G$ (m) | $[3.849 \times 10^{-3},\ 3.889 \times 10^{-3}]$ |
| $m$ (kg) | $[9.036 \times 10^{-6},\ 9.236 \times 10^{-6}]$ |
| $l$ (m) | $[4.18 \times 10^{-3},\ 4.22 \times 10^{-3}]$ |

Table 3: Summary of the uncertain parameters and their numerical values used for propagating uncertainty.

At $k$-th time instant, the box $[\mathbf{d}_k^m] \in \mathbb{IR}^2$ gathering the table tilt measurements, and the initial search space $[\mathbf{q}]_0 = [\hat{\ddot{x}}_{\alpha,k}]_0 \times [\hat{\ddot{y}}_{\alpha,k}]_0 \times [\hat{\ddot{z}}_{\alpha,k}]_0 \in \mathbb{IR}^3$ for the unknown boxes to be computed are defined as follows:

$$[\mathbf{d}_k^m] = [\alpha_{x,k}^m] \times [\alpha_{y,k}^m] \text{ and } [\mathbf{q}]_0 = [-1,1] \times [-1,1] \times [-1,1]. \tag{46}$$

The initial box $[\mathbf{q}]_0$ is large enough for this application case not to remove a single solution. Based on the virtual input shaping done in the previous section, the solution set $\mathbb{S}_k$ is given by:

$$\mathbb{S}_k = \left\{ Q \in [\mathbf{q}]_0 \ \middle|\ \exists\, \mathbf{d} \in [\mathbf{d}_k^m], \begin{array}{l} h_{\mathrm{L}}^x(Q,\mathbf{d}) \in [\hat{\mathcal{I}}_k^x] \\ h_{\mathrm{L}}^y(Q,\mathbf{d}) \in [\hat{\mathcal{I}}_k^y] \\ h_{\mathrm{L}}^z(Q,\mathbf{d}) \in [\hat{\mathcal{I}}_k^z] \end{array} \right\}, \tag{47}$$

The RSEs are disregarded to allow the uncertainty propagation, as they represent unknown dynamics in practice. An incorporated Python script calls the SIVIAP algorithm to estimate the bounds of $\mathbb{S}_k$ using the interval analysis library *PyIbex* [46]. The parametric natural inclusion functions of the shaping models are used for the inclusion tests, and each model is associated with a given forward-backward

contractor. The procedure is repeated at each iteration $k$, with a precision threshold set at $1 \times 10^{-3}$ m/s$^2$. At the end, the box $[\mathbf{q}_k]$ is defined as the interval hull of $\overline{\mathbb{S}}$, i.e. the smallest box that brackets $\overline{\mathbb{S}}$.

### 3.5.3 Simulation results

Although $[\mathbf{q}_k]$ is entirely determined by the uncertainty propagation script, the following analysis focuses only on the first interval component $[\hat{\ddot{x}}_\alpha]$. The estimated bounds of $[\hat{\ddot{x}}_\alpha]$ in open-loop ($i^x = i^y = i^z = 0$) are shown in Fig. 9 and correctly surrounds the theoretical acceleration $\ddot{x}_a$ plotted in blue. This result was to be expected since in Section 3.3, the amplitude of the RSE $\varepsilon_{\mathrm{L}}^x$ is small compared to $\mathcal{I}^x$. This qualitative link between the magnitude of the RSE and the consistency of the computed intervals is valid given that reliable estimated extended state vectors $\hat{X}^e$, $\hat{Y}^e$, $\hat{Z}^e$ and measurements $\alpha_x^m$, $\alpha_y^m$ of the experimental biases are provided for the set inversion. Note that if the intervals introduced for uncertain parameters do not include the values used in the simulation, the computed intervals $[\hat{\ddot{x}}_\alpha]$ may sometimes not correctly surround the theoretical acceleration $\ddot{x}_\alpha$.
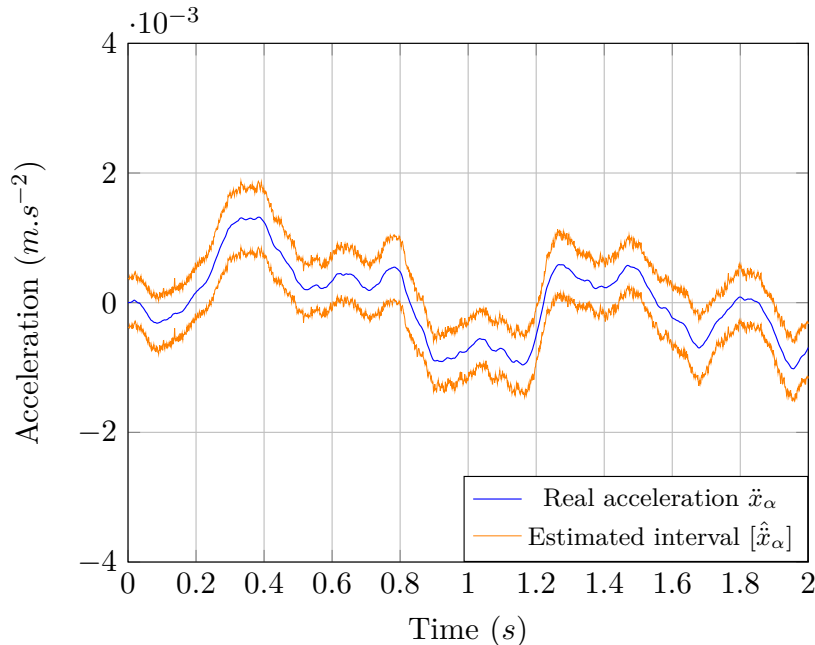


Figure 9: Illustration of the estimated interval $[\hat{\ddot{x}}_\alpha]$ and the theoretical acceleration $\ddot{x}_\alpha$.

## 3.6 Nonlinear shaping model for large oscillations

The previous simulation gave consistent estimates using linear shaping models because small accelerations $\ddot{x}_\alpha$, $\ddot{y}_\alpha$ and $\ddot{z}_\alpha$ were used. The following case study is thus deliberately carried out with large excitation signals in order to illustrate the effectiveness of the nonlinear shaping models, compared to its linearized form under degraded

experimental conditions. The same four-step approach has been adopted, with only the required adjustments presented below. The noise power of the unknown disturbing accelerations $\vec{a}_{ie}$ and tilt angles $\vec{\alpha}$ are increased respectively to $1 \times 10^2$ m$^2$/s$^4$/Hz and $2 \times 10^{-1}$ rad$^2$/Hz in order to generate sufficiently large displacements (see Fig. 10a). In the HOES-LKF, the power spectral density $w_{\text{PSD}}$ that models the virtual input is set to $1 \times 10^6$ A$^2$/Hz. This value had to be increased significantly to correctly observe the virtual input because the pendulum is simulated with relatively large displacements, while the displacement sensor noise still has a low variance $R$. The theoretical virtual input $\mathcal{I}^x$, its estimate $\hat{\mathcal{I}}^x$ and the $3\sigma$ bounds are shown in Fig. 10b.

The SIVIAP algorithm starting boxes are set to $[-100, 100] \times [-100, 100] \times [-100, 100]$ and the precision threshold is tuned to $8 \times 10^{-1}$ m/s$^2$. In the case of large oscillations, the small displacement and small angle assumptions no longer apply, so the virtual input shapes (40) are not sufficiently consistent. More complex shaping models are therefore proposed by considering the nonlinear function $\Delta_{\text{NL}}^x$ given by equation (34), and its equivalents $\Delta_{\text{NL}}^y$ and $\Delta_{\text{NL}}^z$ defined below for the $y$ and $z$-accelerometers. Regarding the $x$-accelerometer, the shaping model $h_{\text{NL}}^x$ is defined as follows:

$$h_{\text{NL}}^x(Q, D) = \frac{1}{b^x}\left[\Delta_{\text{NL}}^x(X, Q, D, i^x) + a_1^x \dot{x} + a_0^x x - b^x i^x\right]. \tag{48}$$

Fig. 11a compares the theoretical output of the shaping models $h_{\text{L}}^x$ and $h_{\text{NL}}^x$ to the virtual input $\mathcal{I}^x$. The related RSEs $\varepsilon_{\text{L}}^x$ and $\varepsilon_{\text{NL}}^x$ are plotted in Fig. 11b. These two figures show that differences are observed when considering larger excitation signals. As expected, the nonlinear shaping model is more consistent with the theoretical virtual input in this case. However, it is not perfectly accurate since uncertain parameters are still taken into account. The nonlinear shaping is repeated for other axes and leads to the following virtual input shapes:

$$\begin{cases} \mathcal{I}^x = \dfrac{1}{b^x}\left[\Delta_{\text{NL}}^x(X, Q, D, i^x) + a_1^x \dot{x} + a_0^x x - b^x i^x\right] + \varepsilon_{\text{NL}}^x \\[2ex] \mathcal{I}^y = \dfrac{1}{b^y}\left[\Delta_{\text{NL}}^y(Y, Q, D, i^y) + a_1^y \dot{y} + a_0^y y - b^y i^y\right] + \varepsilon_{\text{NL}}^y, \\[2ex] \mathcal{I}^z = \dfrac{1}{b^z}\left[\Delta_{\text{NL}}^z(Z, Q, D, i^z) + a_1^z \dot{z} + a_0^z z - b^z i^z\right] + \varepsilon_{\text{NL}}^z \end{cases} \tag{49}$$

in which:

$$\Delta_{\text{NL}}^y(Y, Q, D, i^y) = \frac{2\dot{y}^2 y}{l^2(1 + (\frac{y}{l})^2)} - \frac{l(1 + (\frac{y}{l})^2)}{J}\left[ml_G\Big(\ddot{y}_\alpha \text{c}(\theta_y) + \ddot{z}_\alpha \text{s}(\theta_y)\right. \tag{50}$$

$$\left. + g\big[\text{c}(\theta_y)\text{c}(\alpha_y)\text{s}(\alpha_x) + \text{s}(\theta_y)\text{c}(\alpha_y)\text{c}(\alpha_x)\big]\Big) + K_m^y \theta_y - K_b^y i^y\right] - \frac{K_v^y}{J}\dot{y},$$

28
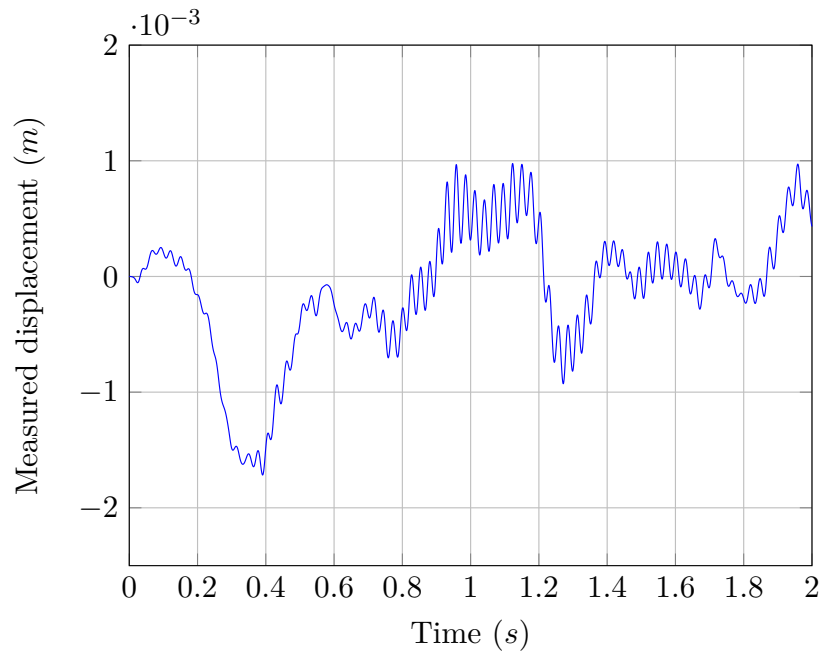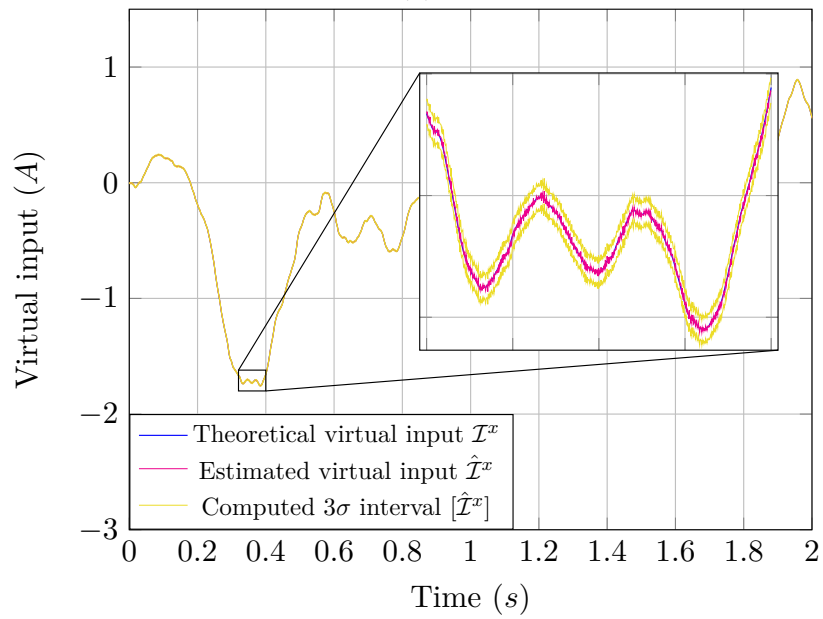
Figure 10: (a) Simulation of the open-loop displacement of the $x$-pendulum excited by large accelerations and tilt angles. (b) Plot of the virtual input $\mathcal{I}^x$, its estimated value $\hat{\mathcal{I}}^x$ and the $3\sigma$ bounds.
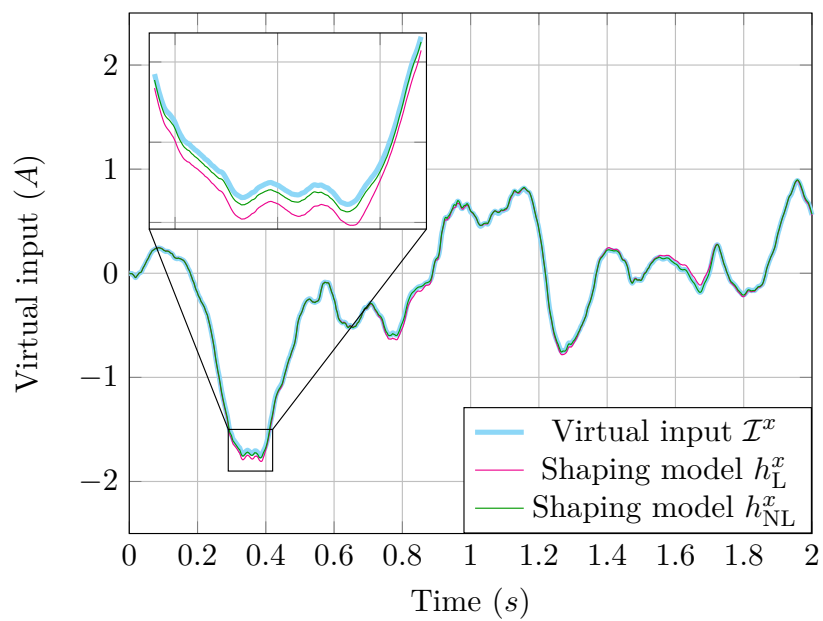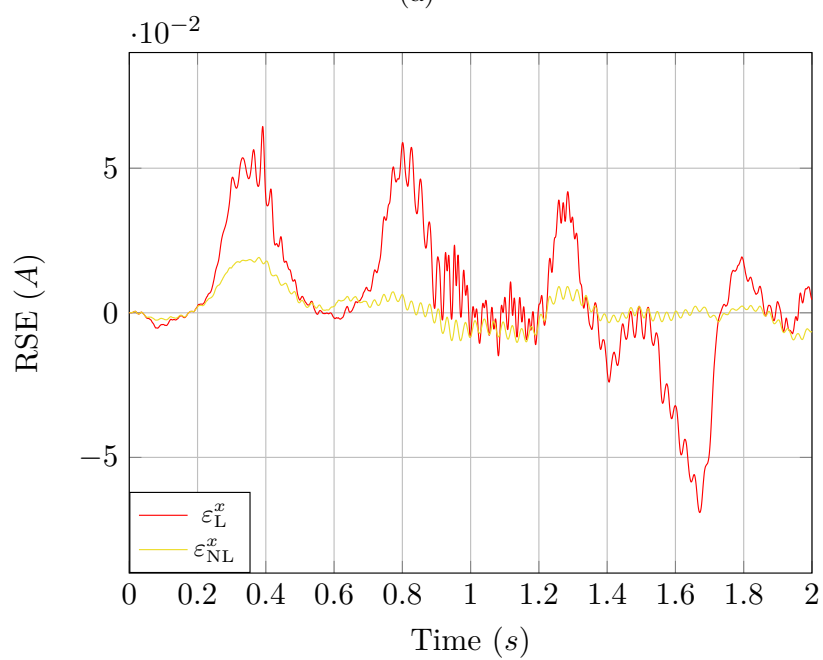
Figure 11: (a) Comparison of the shaping model $h_{\mathrm{L}}^x$ and $h_{\mathrm{NL}}^x$ outputs and the theoretical virtual input value. (b) Plot of the associated RSEs $\varepsilon_{\mathrm{L}}^x$ and $\varepsilon_{\mathrm{NL}}^x$.

$$\Delta_{\mathrm{NL}}^z(Z,Q,D,i^z) = \frac{2\dot{z}^2 z}{l^2(1+(\frac{z}{l})^2)} - \frac{l(1+(\frac{z}{l})^2)}{J}\left[ml_G\Big(\ddot{z}_\alpha \mathrm{c}(\theta_z) + \ddot{x}_\alpha \mathrm{s}(\theta_z)\right. \tag{51}$$

$$\left.- g\big[1 - \mathrm{c}(\theta_z)\mathrm{c}(\alpha_y)\mathrm{c}(\alpha_x) + \mathrm{s}(\theta_z)\mathrm{s}(\alpha_y)\big]\Big) + K_m^z\theta_z - K_b^z i^z\right] - \frac{K_v^z}{J}\dot{z}.$$

with $\theta_y = \mathrm{atan}(y/l)$ and $\theta_z = \mathrm{atan}(z/l)$. These virtual input shapes handle the nonlinearities that may arise with strong excitation signals, resulting in reliable estimated bounds for the unknown accelerations of interest, as illustrated in Fig. 12. Note that the width of the estimated intervals $[\hat{\ddot{x}}_\alpha]$ is smaller compared to those in the previous study because the noise variance $R$ of the interferometer is unchanged while large displacements are simulated. This second scenario highlights the suitability of this methodology for nonlinear systems associated to a nonlinear modeling. In this case, the proposed methodology makes it easy to define a nonlinear shaping model for the virtual input associated with the linear model used to determine the equivalent representation of the system under study. Indeed, the SIVIAP algorithm can handle complex shaping models, as natural inclusion functions can be easily defined. As a result, the range of expressions that can be used to shape a virtual input is wide, and can therefore include serious nonlinearities.
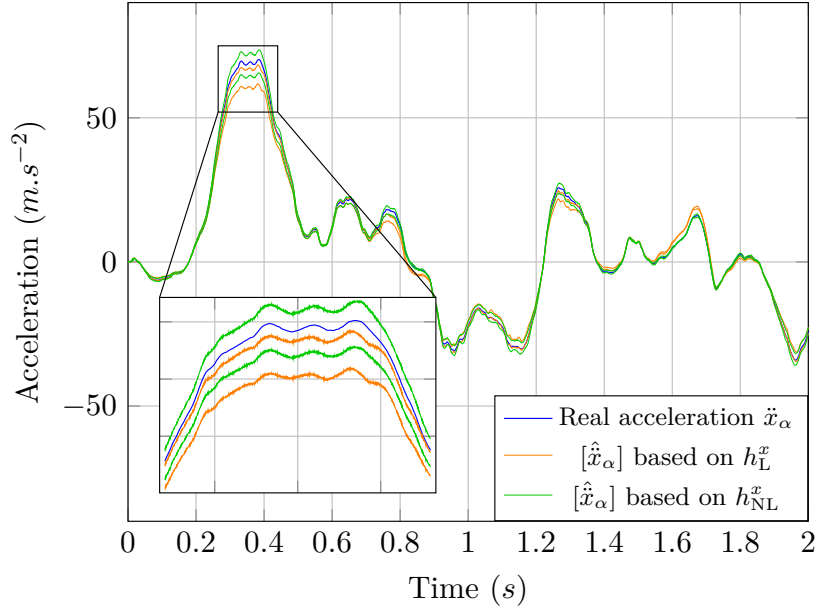


Figure 12: Comparison of the estimated interval $[\hat{\ddot{x}}_\alpha]$ and the theoretical acceleration $\ddot{x}_\alpha$ according to the shaping model used.

# 4 Limitations and outlooks

As with any uncertainty calculation method, the consistency of the computed intervals cannot be guaranteed for dynamic unknown inputs. With regard to the proposed

methodology, this section presents the reasons that can lead to intervals that do not correctly surround the quantities of interest. Ideas for solving or preventing this problem are introduced, and computation optimization is discussed.

## 4.1   Study of the RSE

The unknown RSE represents the differences between the computed output of the shaping model considered and the theoretical value of the virtual input. When solving the set inverse problem (21) in the last step of the methodology, the RSE must be set to zero which may lead to estimation errors. Indeed, its value depends on the consistency of the shaping models used to calculate uncertainty, but also on the reliability of the estimated extended state vector and bias measurements, which cannot be guaranteed in practice, and may result in a non-zero RSE. Moreover, if a significant physical phenomenon has been overlooked in the shaping of the virtual input, or is incorrectly measured, the computed boxes $[\mathbf{q}_k]$ may be incompatible with the unknown quantities of interest. To illustrate this, another look is taken at the previous example with small displacements without considering table tilt angles when determining $h_{\mathrm{L}}^x$, $h_{\mathrm{L}}^y$ and $h_{\mathrm{L}}^z$. The dynamics linked to these angles are therefore necessarily included in the RSEs (see Fig. 13a), which induces an estimation error when setting them to zero to calculate uncertainty. Indeed, the estimated bounds of $[\hat{\ddot{x}}_\alpha]$ plotted in Fig. 13b do not correctly surround $\ddot{x}_\alpha$. In future works, a particular attention will be paid to the study of potential RSEs by examining more closely the spectral content of the input-output signals of the system $(\mathcal{S})$. The idea is to monitor the amplitude of these signals over frequency ranges that are incompatible a priori with those of the quantities of interest and measurement biases. If activity is measured, this means that physical phenomena not taken into account by the shaping models are disturbing the system and will then be contained in the associated RSEs. Fault detection-like approaches are envisaged, with the aim of declaring indicators able to validate or not the computed intervals.

## 4.2   Observer bandwidth

As previously explained, an observer must be implemented in order to estimate the virtual input. However, discrete observers are limited in bandwidth which depends on the observer tuning. A disturbance that is too abrupt will generate a virtual input that is too fast to be estimated correctly. As a result, the assumption that $\mathcal{I}_k^x \in [\hat{\mathcal{I}}_k^x]$ would no longer be valid. Fig. 14 shows the open-loop estimation of the theoretical virtual input when the system is mechanically perturbed by a step input. In this case, the observer cannot follow the fast dynamics of the virtual input during a short period of 25 ms at the time of the step. If the use of a observer is becoming more widespread for metrological applications, its bandwdidth must therefore be carefully adjusted. Otherwise, the calculation of uncertainty must be interrupted during the period when the observer cannot estimate the virtual input properly, or the above-mentioned indicators must invalidate the calculated boxes $[\mathbf{q}_k]$. Starting points to achieve this could be the study of observer dynamics in simulation to determine
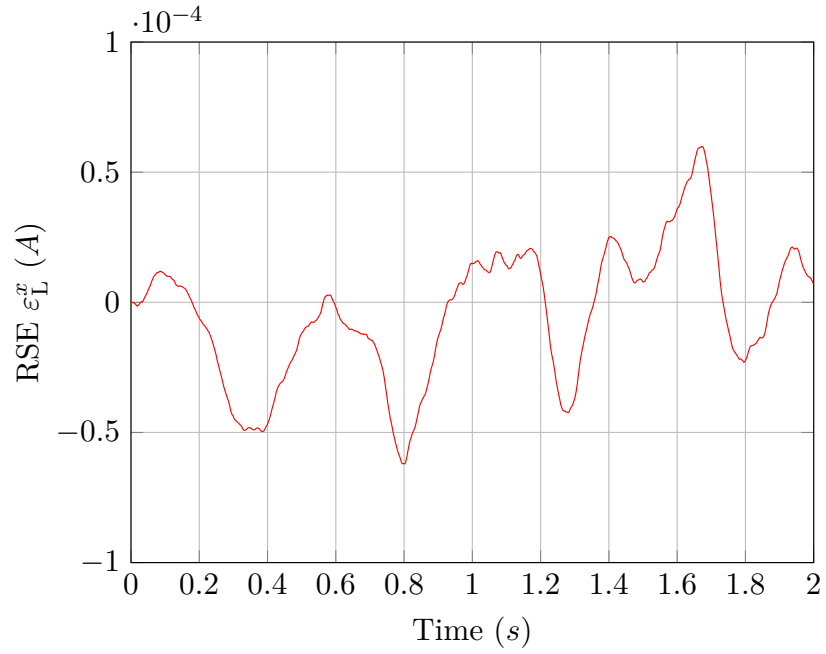
(a)
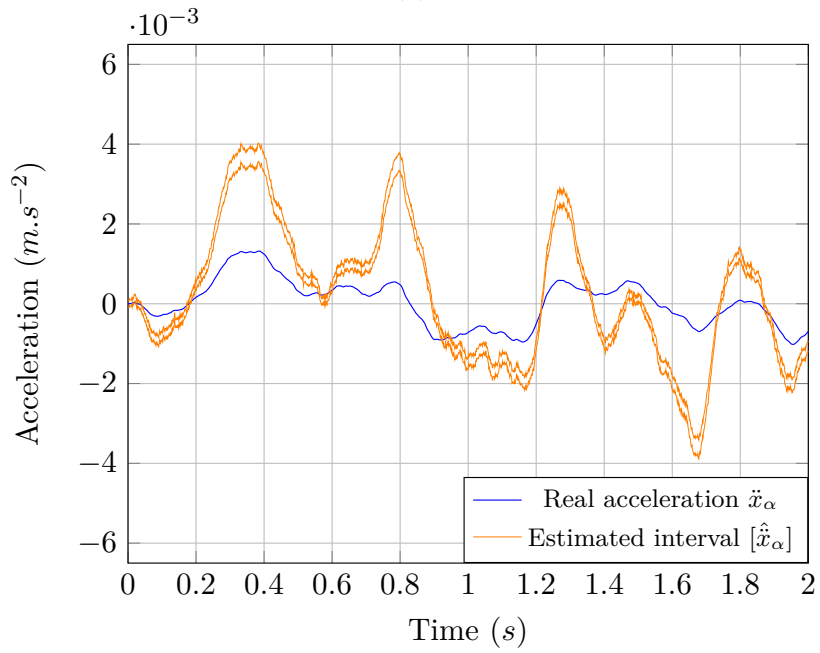


(b)

Figure 13: (a) Plot of the estimated interval $[\hat{\ddot{x}}_\alpha]$ and the theoretical acceleration $\ddot{x}_\alpha$ considering tilt angles. (b) Illustration of the associated RSE.
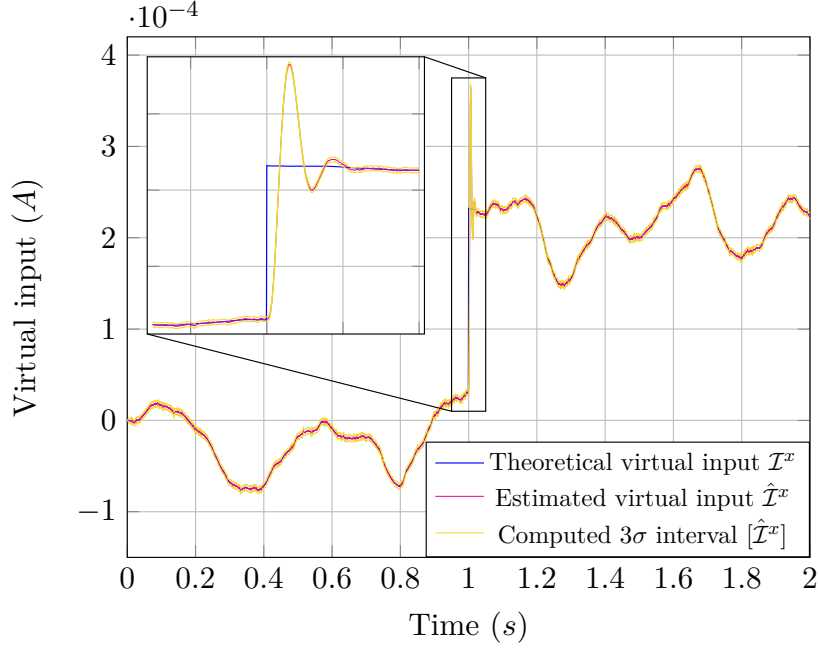
Figure 14: Illustration of the observation issue of the virtual input due to a discrete limited bandwidth.

criteria on the estimated dynamics of the virtual input, the study of the magnitude of closed-loop control command required to counter disturbances with a large transient or the deviation from the displacement reference.

## 4.3 Computation optimization

The SIVIAP algorithm is implemented in this article to compute the boxes $[\mathbf{q}_k]$ that estimate the quantities of interest. However, when the dimensions of the problem become too large, or the precision threshold too refined, such a branch-and-bound algorithm may require a large amount of computing power. A precise representation of the solution set is not essential to determine uncertainty, since only the smallest box that contains $\overline{\mathbb{S}}$ is returned. Several SIVIAP iterations can be avoided by using, for example, an algorithm that directly computes the interval hull of the solution set [43]. Then, the shaping model takes as a parameter, the box $[\mathbf{d}_k^m]$ that lumps the measurement biases. Also, intervals are introduced into the SIVIAP algorithm to account for uncertain parameters. In this case, the natural inclusion function of the shaping model is said to be parametric and uncertain, and corresponds to a *thick inclusion function*. The current implementation of the SIVIAP algorithm handles this particular case but the computation can be optimized since it creates *penumbra*. The penumbra corresponds to regions of the solution set where indeterminate boxes accumulate until the precision threshold is reached. Not all elements in these boxes satisfy the membership tests due to the presence of uncertain variables and parameters in the inclusion function. The theory of thick sets is presented in [47] and may be an interesting perspective to consider in order to reduce the computation time. In

particular, the thick set inversion problem is tackled in [48] using thick separators [49].

# 5 Conclusion

In this article, a new methodology for computing the uncertainties of specific unknown inputs disturbing a nonlinear system has been presented. This method relies on the equivalent representation of a given class of disturbed nonlinear SISO system $(\mathcal{S})$. The principle of equivalent representation is based on a linear model $(\mathcal{M})$ associated with an additive virtual input $\mathcal{I}$. By construction, this additive term gathers all the disturbing unknown inputs and corresponds therefore to the discrepancy the dynamics of $(\mathcal{M})$ compared to $(\mathcal{S})$, which is then estimated by an observer. To distinguish the dynamics of the quantities of interest from the measurement biases, a shaping model describing the dynamics of the virtual input is required. The resulting virtual input shape is finally used to define a set inversion problem, that leads to uncertainty intervals for the unknown quantities to be estimated using interval analysis. The whole approach has been successfully implemented step-by-step in simulation on an uncertain passive accelerometer disturbed by unknown residual vibrations. Prospects have been stated and ongoing works related to the promising impact of closed-loop control will be developed in the future. The development of an alternative methodology for calculating the uncertainty budget of dynamical systems, based on the concept of equivalent representation, is therefore worth considering. A comparative analysis should be carried out in the future to compare its efficiency with other existing approaches when specific unknown inputs have to be estimated with uncertain and disturbed nonlinear dynamical systems. This methodology will be applied to the real experimental setup, and constitutes a key element of the future calculation chain to be implemented on the electromagnetic force balance. The long-term objective is to calibrate the entire experimental setup in relation with NMIs, to guarantee the traceability and reliability of small force measurements and thus to offer new perspectives for small force metrology.

# A Theorem of equivalent representation : Proof

Consider $(\mathcal{S})$, the uncertain disturbed and time-varying SISO nonlinear system introduced in Section 2.1, whose dynamics is described by the following state-space representation:

$$(\mathcal{S}) : \begin{cases} \dot{\mathcal{X}} = f(\mathcal{X}, u, d, t), \\ y = g(\mathcal{X}, u, d, t) \end{cases} \tag{52}$$

in which $\mathcal{X} \in \mathbb{R}^n$ is the state vector, $u \in \mathbb{R}$ is the output of the controller, $d \in \mathbb{R}^\delta$ represents unknown disturbances, $f$ and $g$ are respectively the time-varying evolution and observation functions of $(\mathcal{S})$.

Since it is only known that $f$ and $g$ exist, the proof relies exclusively on the knowledge of $u$ and $y$, the output of $(\mathcal{S})$. An identified, or *a priori* known linear model $(\mathcal{M})$ must be chosen to observe the dynamic of $y$. As in Section 2.1, the model $(\mathcal{M})$ has an imposed structure described by:

$$(\mathcal{M}): \begin{cases} \dot{X}_m = AX_m + Bu, \\ y_m = CX_m \end{cases} \tag{53}$$

with $X_m \in \mathbb{R}^p$, $p > 0$ and $A$, $B$, $C$ given by (3) and (4). In this case, the output $y_m$ of $(\mathcal{M})$ is described by an Ordinary Differential Equation of order $p > 0$:

$$y_m^{(p)} + \sum_{i=0}^{p-1} a_i y_m^{(i)} = bu. \tag{54}$$

**Remark 1** *The choice of $p$ depends on the application. The physical laws that may be used to find an appropriate model often dictate the order of the model. In other cases, when no information or existing model exists, the order $p$ must be consistent with the application. For example, if the purpose is to control the acceleration of a system that has a displacement output, the identified model must be at least of order $p \geq 2$.*

As the two outputs $y$ and $y_m$ have *a priori* different evolutions ~~in~~ over time, it is necessary to establish a formal link between them to describe precisely the real dynamics of $(\mathcal{S})$ thanks to $(\mathcal{M})$. Therefore, their differences are introduced through w:

$$\mathrm{w} \triangleq y - y_m. \tag{55}$$

The assumption that the term w defined in the previous equation is continuous and differentiable is made. The derivatives of $y_m$ in (54) can thus be computed and replaced:

$$y^{(p)} - \mathrm{w}^{(p)} + \sum_{i=0}^{p-1} a_i(y^{(i)} - \mathrm{w}^{(i)}) = bu. \tag{56}$$

Equation (56) can be ordered as follows:

$$y^{(p)} + \sum_{i=0}^{p-1} a_i y^{(i)} = bu + \mathrm{w}^{(p)} + \sum_{i=0}^{p-1} a_i \mathrm{w}^{(i)}. \tag{57}$$

An additional input $\mathcal{I}$, homogeneous to $u$, can thus be introduced as a function of w and its derivatives:

$$b\mathcal{I} \triangleq \mathrm{w}^{(p)} + \sum_{i=0}^{p-1} a_i \mathrm{w}^{(i)}. \tag{58}$$

The latter expression has no physical meaning but rather is a mathematical construction that gathers the dynamical differences, observed through the identified model,

between the outputs $y$ and $y_m$. This additional term, called virtual input can be written in (57):

$$y^{(p)} + \sum_{i=0}^{p-1} a_i y^{(i)} = bu + b\mathcal{I}. \tag{59}$$

Therefore, the accurate dynamic of $y$ and its $p$ successive derivatives is consistently reproduced by the LTI model $(\mathcal{M})$, thanks to $\mathcal{I}$. To conclude this first appendix, the following state vector $X$ is introduced:

$$X = \begin{bmatrix} y & \dot{y} & \dots & y^{(p-1)} \end{bmatrix}^T \in \mathbb{R}^p. \tag{60}$$

The latter equivalent model (59) can therefore be stated under the form of a state-space representation:

$$\begin{cases} \dot{X} = AX + B(u + \mathcal{I}), \\ y = CX \end{cases} \tag{61}$$

in which $A \in \mathbb{R}^{p \times p}$, $B \in \mathbb{R}^{p \times 1}$, $C \in \mathbb{R}^{1 \times p}$ are the following perfectly known state, input and output matrices:

$$A = \begin{bmatrix} 0 & 1 & 0 & 0 & \dots & 0 \\ 0 & 0 & 1 & 0 & \dots & 0 \\ & & & \ddots & & \\ 0 & 0 & 0 & \dots & 0 & 1 \\ -a_0 & \dots & & & -a_{p-1} \end{bmatrix}, \quad B = \begin{bmatrix} 0 \\ 0 \\ \vdots \\ 0 \\ b \end{bmatrix}, \tag{62}$$

$$C = \begin{bmatrix} 1 & 0 & \dots & 0 \end{bmatrix}.$$

# B  Synthesis of the discrete HOES-LKF

This appendix presents the design of the Higher Order Extended State Linear Kalman Filter (HOES-LKF) used in the application example. The starting point of the following development is the equivalent representation (31) of the nonlinear system $(\mathcal{S})$ in which $X = \begin{bmatrix} x & \dot{x} \end{bmatrix}^T$, and where the numerical values have been replaced with $a_0^x$, $a_1^x$ and $b^x$ :

$$\begin{cases} \dot{X} &= \begin{bmatrix} 0 & 1 \\ -a_0^x & -a_1^x \end{bmatrix} X + \begin{bmatrix} 0 \\ b^x \end{bmatrix} (i^x + \mathcal{I}^x), \\ x &= \begin{bmatrix} 1 & 0 \end{bmatrix} X. \end{cases} \tag{63}$$

Based on the typical implementation of ESO, the unknown input, i.e. the virtual input $\mathcal{I}^x$ in this case, is added to the state vector along with its first derivative to form a higher order extended state observer. The state vector $X^e \in \mathbb{R}^4$ is thus defined as:

$$X^e = \begin{bmatrix} x & \dot{x} & \mathcal{I}^x & \dot{\mathcal{I}}^x \end{bmatrix}^T \tag{64}$$

and leads to the following associated extended state-space representation:

$$\begin{cases} \dot{X}^e = \mathcal{A}X^e + \mathcal{B}i^x + \mathcal{M}\ddot{\mathcal{I}}^x, \\ x = \mathcal{C}X^e \end{cases} \tag{65}$$

where

$$\mathcal{A} = \begin{bmatrix} 0 & 1 & 0 & 0 \\ -a_0^x & -a_1^x & b^x & 0 \\ 0 & 0 & 0 & 1 \\ 0 & 0 & 0 & 0 \end{bmatrix}, \mathcal{B} = \begin{bmatrix} 0 \\ b^x \\ 0 \\ 0 \end{bmatrix}, \mathcal{M} = \begin{bmatrix} 0 \\ 0 \\ 0 \\ 1 \end{bmatrix}, \tag{66}$$

$$\mathcal{C} = \begin{bmatrix} 1 & 0 & 0 & 0 \end{bmatrix}.$$

On the one hand, the behavior of the virtual input is assumed to be unknown, which results in totally unpredictable dynamics. On the other hand, the noise present on the input of the system must be taken into account in the uncertainty calculation associated to the extended state estimation. White Gaussian stochastic processes $\omega$ and $\omega_i$ with zero mean and infinite variance are used to represent the unpredictable behavior of $\ddot{\mathcal{I}}^x$ and to model the noise added on the input current $i^x$:

$$\begin{cases} \ddot{\mathcal{I}}^x = \omega, \\ i^x = \mathrm{i}^{x,c} + \omega_i. \end{cases} \tag{67}$$

The current $\mathrm{i}^{x,c}$ is the deterministic value of the input current given to the controlled current generator. Each scalar stochastic process noise $\omega$ and $\omega_i$ is respectively characterized by its constant power spectral density $w_{\mathrm{PSD}} \in \mathbb{R}$ and $w_{\mathrm{PSD}i} \in \mathbb{R}$. The stochastic modeling of (63) that now includes both the virtual input dynamics and the current noise model is:

$$\begin{cases} \dot{X}^e = \mathcal{A}X^e + \mathcal{B}\mathrm{i}^{x,c} + \mathcal{B}\omega_i + \mathcal{M}\omega, \\ x = \mathcal{C}X^e. \end{cases} \tag{68}$$

The two scalar stochastic processes are then gathered in $\Omega \in \mathbb{R}^2$:

$$\begin{cases} \dot{X}^e = \mathcal{A}X^e + \mathcal{B}\mathrm{i}^{x,c} + \delta\Omega, \\ x = \mathcal{C}X^e. \end{cases} \tag{69}$$

with

$$\delta = \begin{bmatrix} \mathcal{B} & \mathcal{M} \end{bmatrix} \in \mathbb{R}^{4 \times 2}, \ \Omega = \begin{bmatrix} \omega_i & \omega \end{bmatrix}^T. \tag{70}$$

To implement a discrete LKF, a discretization of (69) is done using a Zero-Order Hold (ZOH) on the input at a period $T_s$. With $y_k^x$ the discretized output of the filter provided with a sensor corrupted by the discrete-time band-limited white Gaussian noise $v_k$ with zero mean and variance $R \in \mathbb{R}$, the discrete stochastic evolution of $X_k^e$ and the output measurement evolution are represented by:

$$\begin{cases} X_{k+1}^e = \mathcal{F}X_k^e + \mathcal{G}\mathrm{i}_k^{x,c} + \Omega_k, \\ x_k = \mathcal{C}X_k^e + v_k, \end{cases} \tag{71}$$

$$\mathcal{F} = e^{\mathcal{A}T_s}, \ \mathcal{G} = \int_0^{T_s} e^{\mathcal{A}t}\mathcal{B}dt$$

in which $\Omega_k$ is a band-limited white Gaussian process noise with a zero-mean and a covariance matrix $Q$ given by:

$$Q = E\left[\Omega_k \, \Omega_k^T\right] = \int_0^{T_s} e^{\mathcal{A}t} \delta W \delta^T e^{\mathcal{A}^T t} dt,$$

$$\text{where} \; : W = \begin{bmatrix} w_{\text{PSD}i} & 0 \\ 0 & w_{\text{PSD}} \end{bmatrix}. \tag{72}$$

As (71) is a linear Gaussian stochastic process, its state $X_k^e$ can be observed with a LKF. Defining an initial estimated extended state $\hat{X}_0^e$ and an initial covariance matrix $P_0$, the prediction and update steps of the HOES-LKF are given by the classical discrete time-varying linear Kalman filter equations:

$$\begin{aligned}
\hat{X}_{k|k-1}^e &= \mathcal{F}\hat{X}_{k-1}^e + \mathcal{G}\text{i}_{k-1}^{x,c}, \\
P_{k|k-1} &= \mathcal{F}P_{k-1}\mathcal{F}^T + Q, \\
K_k &= P_{k|k-1}\mathcal{C}^T(\mathcal{C}P_{k|k-1}\mathcal{C}^T + R)^{-1}, \\
\hat{X}_k^e &= \hat{X}_{k|k-1}^e + K_k(\text{x}_k^m - \mathcal{C}\hat{X}_{k|k-1}^e), \\
P_k &= (I_4 - K_k\mathcal{C})P_{k|k-1}
\end{aligned} \tag{73}$$

with $\text{x}_k^m$ corresponding to the actual output measurement at time $t_k$. The estimated virtual input $\mathcal{I}^x$ is the third component of $X_k^e$ and its associated uncertainty can thus be deduced from the third diagonal component of the covariance matrix $P_k$.

# Acknowledgment

# References

[1] S. Romero-Diez, L. Hantsche, J. M. Pearl, D. L. Hitt, M. R. McDevitt, and P. C. Lee, "A single-use microthruster concept for small satellite attitude control in formation-flying applications," *Aerospace*, vol. 5, no. 4, 2018.

[2] T. Namazu, "Mechanical property measurement of micro/nanoscale materials for mems: A review," *IEEJ Transactions on Electrical and Electronic Engineering*, vol. 18, no. 3, pp. 308–324, 2023.

[3] W. Liu, Y. Guo, K. Wang, X. Zhou, Y. Wang, J. Lü, Z. Shao, J. Hu, D. M. Czajkowsky, and B. Li, "Atomic force microscopy-based single-molecule force spectroscopy detects dna base mismatches," *Nanoscale*, vol. 11, pp. 17206–17210, 2019.

[4] M.-S. Kim, J.-H. Choi, Y.-K. Park, and J.-H. Kim, "Atomic force microscope cantilever calibration device for quantified force metrology at micro- or nanoscale regime: the nano force calibrator (nfc)," *Metrologia*, vol. 43, p. 389, sep 2006.

[5] J.-H. Choi, M.-S. Kim, Y.-K. Park, and M.-S. Choi, "Quantum-based mechanical force realization in piconewton range," *Applied Physics Letters*, vol. 90, p. 073117, 02 2007.

[6] S.-J. Chen and S.-S. Pan, "A force measurement system based on an electrostatic sensing and actuating technique for calibrating force in a micronewton range with a resolution of nanonewton scale," *Measurement Science and Technology*, vol. 22, p. 045104, 03 2011.

[7] J. Pratt, J. Kramar, D. Newell, and D. Smith, "Review of si traceable force metrology for instrumented indentation and atomic force microscopy," *Measurement Science and Technology*, vol. 16, p. 2129, 09 2005.

[8] C. Jones and R. Leach, "Review of low force transfer artefact technologies," 01 2008.

[9] K. Fukuzawa, T. Ando, M. Shibamoto, Y. Mitsuya, and H. Zhang, "Monolithically fabricated double-ended tuning-fork-based force sensor," *Journal of Applied Physics*, vol. 99, p. 094901, 2006.

[10] C. Jones, D. Chetwynd, J. Singh, and R. Leach, "Concept and modelling of a novel active triskelion low force transfer artefact," 05 2011.

[11] M.-s. Kim and Y.-K. Park, "Millimeter-scale piezoresistive cantilevers for accurate force measurements at the nano-newton level," *MAPAN*, vol. 28, 12 2013.

[12] F. Amokrane, *Contribution à l'observation robuste des systèmes dynamiques incertains : application à la métrologie des faibles forces*. Theses, Université Bourgogne Franche-Comté, Jan. 2021.

[13] V. Nesterov, "Facility and methods for the measurement of micro and nano forces in the range below 10-5 n with a resolution of 10-12 n (development concept)," *Measurement Science and Technology*, vol. 18, p. 360, 01 2007.

[14] P. Sun, M. Zhao, J. Jiang, Y. Zheng, Y. Han, and L. Song, "The differential method for force measurement based on electrostatic force," *Journal of Sensors*, vol. 2017, pp. 1–7, 05 2017.

[15] BIPM, IEC, IFCC, ILAC, ISO, IUPAC, IUPAP, and OIML, "Evaluation of measurement data — Guide to the expression of uncertainty in measurement." Joint Committee for Guides in Metrology, JCGM 100:2008.

[16] BIPM, IEC, IFCC, ILAC, ISO, IUPAC, IUPAP, and OIML, "Evaluation of measurement data — Supplement 1 to the "Guide to the expression of uncertainty in measurement" — Propagation of distributions using a Monte Carlo method." Joint Committee for Guides in Metrology, JCGM 101:2008.

[17] BIPM, IEC, IFCC, ILAC, ISO, IUPAC, IUPAP, and OIML, "Evaluation of measurement data — Supplement 2 to the "Guide to the expression of uncertainty in measurement" — Extension to any number of output quantities." Joint Committee for Guides in Metrology, JCGM 102:2011.

[18] BIPM, IEC, IFCC, ILAC, ISO, IUPAC, IUPAP, and OIML, "Guide to the expression of uncertainty in measurement — Part 6: Developing and using measurement models." Joint Committee for Guides in Metrology, JCGM GUM-6:2020.

[19] I. Lira, "The gum revision: the bayesian view toward the expression of measurement uncertainty," *European Journal of Physics*, vol. 37, p. 025803, feb 2016.

[20] S. Eichstädt, V. Wilkens, A. Dienstfrey, P. Hale, B. Hughes, and C. Jarvis, "On challenges in the uncertainty evaluation for time-dependent measurements," *Metrologia*, vol. 53, p. S125, jun 2016.

[21] S. Eichstädt, K. Ruhm, and A. Shestakov, "Dynamic measurement and its relation to metrology, mathematical theory and signal processing: a review," *Journal of Physics: Conference Series*, vol. 1065, p. 212018, 08 2018.

[22] R. E. Kalman, "A New Approach to Linear Filtering and Prediction Problems," *Journal of Basic Engineering*, vol. 82, pp. 35–45, 03 1960.

[23] D. Luenberger, "Observing the state of a linear system," *Military Electronics, IEEE Transactions on*, vol. MIL8, pp. 74 – 80, 05 1964.

[24] S. R. Kou, D. L. Elliott, and T. J. Tarn, "Exponential observers for nonlinear dynamic systems," *Information and Control*, vol. 29, no. 3, pp. 204–216, 1975.

[25] Y. Song and J. W. Grizzle, "The extended kalman filter as a local asymptotic observer for nonlinear discrete-time systems," in *1992 American Control Conference*, pp. 3365–3369, 1992.

[26] M. Zeitz, "The extended luenberger observer for nonlinear systems," *Systems & Control Letters*, vol. 9, no. 2, pp. 149–156, 1987.

[27] I. Peñarrocha, R. Sanchis, and P. Albertos, "H-infinity observer design for a class of nonlinear discrete systems," *European Journal of Control*, vol. 15, no. 2, pp. 157–165, 2009.

[28] B. Yi, R. Ortega, and W. Zhang, "On state observers for nonlinear systems: A new design and a unifying framework," *IEEE Transactions on Automatic Control*, vol. 64, no. 3, pp. 1193–1200, 2019.

[29] A. Radke and Z. Gao, "A survey of state and disturbance observers for practitioners," in *2006 American Control Conference*, pp. 6 pp.–, 2006.

[30] W.-H. Chen, J. Yang, L. Guo, and S. Li, "Disturbance-observer-based control and related methods—an overview," *IEEE Transactions on Industrial Electronics*, vol. 63, no. 2, pp. 1083–1095, 2016.

[31] P. Yu, K.-Z. Liu, X. Liu, X. Li, M. Wu, and J. She, "Analysis of equivalent-input-disturbance-based control systems and a coordinated design algorithm for uncertain systems," *International Journal of Robust and Nonlinear Control*, vol. 31, no. 5, pp. 1755–1773, 2021.

[32] F. Amokrane, E. Piat, J. Abadie, A. Drouot, and J. A. Escareno, "State Observation of a Specific Class of Unknown Nonlinear SISO Systems using Linear Kalman Filtering," in *Conference on Decision and Control*, (Nice, France), Dec. 2019.

[33] J. Han, "A Class of Extended State Observers for Uncertain Systems," *Control and Decision*, vol. 10, no. 1, pp. 85–88, 1995.

[34] H. Jingqing, "Auto-disturbances-rejection controller and its applications," *Control and decision*, vol. 13, no. 1, pp. 19–23, 1998.

[35] J.-H. She, M. Fang, Y. Ohyama, H. Hashimoto, and M. Wu, "Improving disturbance-rejection performance based on an equivalent-input-disturbance approach," *IEEE Transactions on Industrial Electronics*, vol. 55, no. 1, pp. 380–389, 2008.

[36] X. Wang, C. P. Tan, L. Liu, and Q. Qi, "A novel unknown input interval observer for systems not satisfying relative degree condition," *International Journal of Robust and Nonlinear Control*, vol. 31, no. 7, pp. 2762–2782, 2021.

[37] N. Meslem, A. Hably, T. Raïssi, and Z. Wang, "Reliable unknown input observer for continuous-time linear systems," *IFAC-PapersOnLine*, vol. 55, no. 6, pp. 248–253, 2022. 11th IFAC Symposium on Fault Detection, Supervision and Safety for Technical Processes SAFEPROCESS 2022.

[38] X. Fan, W. Zhang, and X. Li, "Fault detection and isolation based on unknown input set-membership observer," in *2020 39th Chinese Control Conference (CCC)*, pp. 4066–4071, 2020.

[39] M. Billot, E. Piat, J. Abadie, and P. Stempflé, "External mechanical disturbances compensation with a passive differential measurement principle in nanoforce sensing using diamagnetic levitation.," *Sensors and Actuators A: Physical*, vol. 238, pp. 266–275, 2016.

[40] R. E. Moore, R. B. Kearfott, and M. J. Cloud, *Introduction to Interval Analysis*. Society for Industrial and Applied Mathematics, 2009.

[41] L. Jaulin, *Le calcul ensembliste par analyse par intervalles et ses applications*. Habilitation à diriger des recherches, Université d'Angers, Feb. 2000.

[42] L. Jaulin and E. Walter, "Set inversion via interval analysis for nonlinear bounded-error estimation," *Automatica*, vol. 29, no. 4, pp. 1053–1064, 1993.

[43] L. Jaulin, "Interval constraint propagation with application to bounded-error estimation," *Automatica*, vol. 36, no. 10, pp. 1547–1552, 2000.

[44] G. Chabert and L. Jaulin, "Contractor programming," *Artificial Intelligence*, vol. 173, no. 11, pp. 1079–1100, 2009.

[45] F. Benhamou, F. Goualard, L. Granvilliers, and J.-F. Puget, "Revising hull and box consistency.," pp. 230–244, 01 1999.

[46] B. Desrochers, T. Le Mézo, M. Saad Ibn Seddik, and S. Rohou, "PyIbex : A Python binding for ibex-lib," Version 1.9.2 (Nov 1, 2020).

[47] B. Desrochers, *Simultaneous localization and mapping in unstructured environments : a set-membership approach*. Theses, ENSTA Bretagne - École nationale supérieure de techniques avancées Bretagne, May 2018.

[48] B. Desrochers and L. Jaulin, "Thick set inversion," *Artificial Intelligence*, vol. 249, pp. 1–18, 2017.

[49] L. Jaulin and B. Desrochers, *Thick Separators*, pp. 125–131. 03 2020.